

Neural Parameter Estimation with Incomplete Data

Matthew Sainsbury-Dale^{1,2}, Andrew Zammit-Mangion², Noel Cressie², and
Raphaël Huser¹

¹Statistics Program, Computer, Electrical and Mathematical Sciences and Engineering Division,
King Abdullah University of Science and Technology (KAUST), Saudi Arabia

²School of Mathematics and Applied Statistics, University of Wollongong, Australia

Abstract

Advancements in artificial intelligence (AI) and deep learning have led to neural networks being used to generate lightning-speed answers to complex questions, to paint like Monet, or to write like Proust. Leveraging their computational speed and flexibility, neural networks are also being used to facilitate fast, likelihood-free statistical inference. However, it is not straightforward to use neural networks with data that for various reasons are incomplete, which precludes their use in many applications. A recently proposed approach to remedy this issue inputs an appropriately padded data vector and a vector that encodes the missingness pattern to a neural network. While computationally efficient, this “masking” approach can result in statistically inefficient inferences. Here, we propose an alternative approach that is based on the Monte Carlo expectation-maximization (EM) algorithm. Our EM approach is likelihood-free, substantially faster than the conventional EM algorithm as it does not require numerical optimization at each iteration, and more statistically efficient than the masking approach. This research represents a prototype problem that indicates how improvements could be made in AI by introducing Bayesian statistical thinking. We compare the two approaches to missingness using simulated incomplete data from two models: a spatial Gaussian process model, and a spatial Potts model. The utility of the methodology is shown on Arctic sea-ice data and cryptocurrency data.

Keywords: amortized inference, likelihood-free inference, Monte Carlo EM algorithm, neural Bayes estimator, simulation-based inference

1 Introduction

Artificial intelligence (AI) and deep learning have spurred significant advancements in recent years, revolutionizing fields ranging from image recognition to natural language processing, and enabling transformative technologies like ChatGPT (OpenAI, 2023). These breakthroughs are profoundly influencing how we work, communicate, and create, leaving an indelible mark on society. In parallel, the last decade has seen growing interest in the use of neural networks for likelihood-free inference, which is often used in statistical or physical

models for which the likelihood function is unavailable or computationally intractable (Diggle and Gratton, 1984; Cranmer et al., 2020). Neural networks are being used to approximate the likelihood function (e.g., Papamakarios et al., 2019), the likelihood-to-evidence ratio (e.g., Hermans et al., 2020; Thomas et al., 2022; Walchessen et al., 2024), the posterior distribution (e.g., Greenberg et al., 2019; Gonçalves et al., 2020; Radev et al., 2022; Pacchiardi and Dutta, 2022; Ramesh et al., 2022; Maceda et al., 2024), and both the likelihood and the posterior distribution simultaneously (e.g., Glöckler et al., 2022; Radev et al., 2023); see Zammit-Mangion et al. (2025) for a recent review. In this work, we consider neural Bayes estimators (NBEs; Sainsbury-Dale et al., 2024), which are neural networks that map data to a point summary of the posterior distribution. These estimators are likelihood-free and amortized, in the sense that, after an initial set-up cost, inference from observed data can be made in a fraction of the time required by conventional approaches. NBEs have been used to make fast inference with models for population genetics (Flagel et al., 2018), financial options (Hernandez, 2017; Horvath et al., 2021), cognitive processes (Pan et al., 2024), spatial processes (Gerber and Nychka, 2021; Lenzi et al., 2023; Sainsbury-Dale et al., 2024, 2025; Richards et al., 2025; Tsyrlunikov and Sotskiy, 2024; Villazón et al., 2024; Wang and Genton, 2024), and spatio-temporal processes (Dell’Oro and Gaetan, 2024).

NBEs represent a promising approach to inference, yet significant challenges remain that hinder their widespread adoption. One of the key challenges is their application to the often-encountered “incomplete data” setting, where the structure of the available data renders the use of conventional neural networks problematic. Consider, for instance, remote-sensing data collected over a regular grid. If all pixels are observed (i.e., no data are missing), one can readily construct an NBE of a geophysical parameter using a standard convolutional neural network (CNN). However, this parsimonious, efficient architecture cannot be used directly if data are missing (e.g., due to cloud cover). Similarly, in medical and health applications, incomplete data often arise in electronic health records, where patients may have missing clinical or demographic information, or in clinical trials, where participants may drop out or miss scheduled evaluations. In financial applications, the valuation of options or other financial derivatives may involve historical data with missing observations caused by, for example, market closures or differing inception dates of assets. In these scenarios, the application of NBEs requires novel methods to handle incomplete data in a statistically principled manner.

A recently proposed method for handling missing data involves “masking” (Wang et al., 2024; Gloeckler et al., 2024). In this approach, the neural network takes as input the complete data with missing elements replaced by zero (or some other fixed constant) and a binary vector encoding the missingness pattern. Although computationally efficient, this method has some drawbacks. For instance, incorporating the missingness pattern as an additional input results in a more challenging learning task. Further, the approach necessitates a stochastic model for the missingness mechanism and, as we will show, misspecification of this model can lead to biased and suboptimal inference.

Statistical efficiency is as important as computational efficiency, and in this research we consider both in a prototype problem that indicates where improvements could be made in AI by introducing statistical inferential tools. Specifically, we propose to facilitate the use of NBEs in the presence of missing data by leveraging methods developed for incomplete-data problems, where the data are challenging to analyze directly but their analysis be-

comes tractable through appropriate data augmentation. Several algorithms have been developed to address such problems, among which the most prominent are the expectation-maximization (EM) algorithm for maximum-likelihood or maximum-a-posteriori (MAP) estimation (Dempster et al., 1977) and the data-augmentation algorithm for posterior sampling (Tanner and Wong, 1987). These approaches exploit likelihood functions or posterior distributions, respectively, that are intractable for the observed incomplete data but tractable under data augmentation. There is a strong parallel between the classical incomplete-data problem and that faced in neural inference: there are situations where neural-network architectures are complex or unavailable for observed incomplete data, but are simpler, more parsimonious, and easier to train, under data augmentation. Note that, in machine learning “data augmentation” typically refers to methods that artificially increase the amount of data used to train neural networks; here we use it exclusively to refer to the process of augmenting data with latent random variables.

Building on this connection, we introduce an implementation of NBEs for incomplete data using data augmentation. Specifically, we develop a type of Monte Carlo EM algorithm (Wei and Tanner, 1990; Levine and Casella, 2001) where, after conditional simulation of the missing data, the remaining components of the usual E- and the M-steps are obtained almost instantaneously with an NBE trained to approximate the MAP estimator. MAP estimators are prominent in areas as diverse as image analysis (Hardie et al., 2004) and plant breeding (Montesinos-López et al., 2020). Our EM approach to neural Bayes estimation is likelihood-free and does not require numerical optimization at each iteration, making it much faster than the standard EM algorithm. Critically, the NBE is trained on, and applied to, complete (augmented) data only, which we show alleviates the drawbacks of the masking approach discussed above. However, our EM approach has its own limitations, as it requires conditional simulation and is slower than the masking approach due to its iterative nature. Thus, our EM approach is more statistically efficient than the masking approach but it is not as computationally efficient, which emerges clearly in our experiments. Both methods have been incorporated into the user-friendly open-source software package **NeuralEstimators** (Sainsbury-Dale, 2024), which is available in Julia and R.

The remainder of this article is organized as follows. In Section 2, we review NBEs, discuss and give new insights on the masking approach of Wang et al. (2024), and introduce our EM approach. In Section 3, we conduct simulation studies to investigate the strengths and weaknesses of these two approaches for dealing with missing data. In Section 4, we apply our methodology to an analysis of Arctic sea-ice data. In Section 5, we give conclusions and outline avenues for future research. Supplementary material is also available that contains further theoretical details and simulations, more figures, and an additional application to cryptocurrency data. Code that reproduces all results in the manuscript is available from <https://github.com/msainsburydale/NeuralIncompleteData>.

2 Methodology

In Section 2.1, we review NBEs. (For a more comprehensive introduction, see Sainsbury-Dale et al., 2024.) In Section 2.2, we present the masking approach of Wang et al. (2024) for missing data and, in Section 2.3, we describe our alternative EM approach.

2.1 Neural Bayes estimators

The goal of parametric point estimation is to estimate a p -dimensional parameter $\boldsymbol{\theta} \in \Theta$ from data $\mathbf{Z} \in \mathcal{Z}$ using an estimator, $\hat{\boldsymbol{\theta}} : \mathcal{Z} \rightarrow \Theta$. For ease of exposition, we let $\Theta \subseteq \mathbb{R}^p$ and $\mathcal{Z} \subseteq \mathbb{R}^n$, although the approaches we describe generalize to other spaces. A ubiquitous decision-theoretic approach to the construction of estimators is based on average-risk optimality (e.g., [Lehmann and Casella, 1998](#), Ch. 4; [Robert, 2007](#), Ch. 4). Consider a loss function $L : \Theta \times \Theta \rightarrow [0, \infty)$ and, for ease of exposition, assume that the prior measure for $\boldsymbol{\theta}$ admits a density $\pi(\cdot)$ with respect to Lebesgue measure on \mathbb{R}^p . Then the Bayes risk of the estimator $\hat{\boldsymbol{\theta}}(\cdot)$ is

$$r(\hat{\boldsymbol{\theta}}(\cdot)) \equiv \int_{\Theta} \int_{\mathcal{Z}} L(\boldsymbol{\theta}, \hat{\boldsymbol{\theta}}(\mathbf{z})) f_{\mathbf{Z}|\boldsymbol{\theta}}(\mathbf{z} | \boldsymbol{\theta}) \pi(\boldsymbol{\theta}) d\mathbf{z} d\boldsymbol{\theta}, \quad (1)$$

where here and throughout, for generic random quantities A and B , we use $f_{A|B}(\cdot | \cdot)$ to denote the conditional probability density/mass function of A given B , and $f_A(\cdot)$ to denote the marginal probability density/mass function of A . Any minimizer of (1) is said to be a *Bayes estimator* with respect to $L(\cdot, \cdot)$ and $\pi(\cdot)$.

Bayes estimators are functionals of the posterior distribution (e.g., the Bayes estimator under quadratic loss is the posterior mean) and are often unavailable in closed form. However, since estimators are mappings from the sample space \mathcal{Z} to the parameter space Θ , Bayes estimators could, in principle, be approximated well by a sufficiently flexible function. Recently, motivated by universal-function-approximation theorems (e.g., [Hornik et al., 1989](#); [Zhou, 2020](#)) and the speed at which they can be evaluated, neural networks have been used to approximate Bayes estimators. Let $\hat{\boldsymbol{\theta}}_{\boldsymbol{\gamma}} : \mathcal{Z} \rightarrow \Theta$ denote a neural network parameterized by $\boldsymbol{\gamma}$, that is,

$$\hat{\boldsymbol{\theta}}_{\boldsymbol{\gamma}}(\mathbf{Z}) = \mathbf{g}(\mathbf{Z}; \boldsymbol{\gamma}) = (\mathbf{g}_J \circ \mathbf{g}_{J-1} \circ \cdots \circ \mathbf{g}_1)(\mathbf{Z}; \boldsymbol{\gamma}), \quad \mathbf{Z} \in \mathcal{Z}, \quad (2)$$

where $\mathbf{g}(\cdot; \boldsymbol{\gamma})$ is a nonlinear function obtained by composition of functions $\mathbf{g}_j(\cdot; \boldsymbol{\gamma}_j)$, $j = 1, \dots, J$ parameterized by $\boldsymbol{\gamma} = (\boldsymbol{\gamma}'_1, \dots, \boldsymbol{\gamma}'_J)'$, and ‘ \circ ’ denotes function composition. Then, a Bayes estimator may be approximated by substituting $\boldsymbol{\gamma}^*$ into (2), where

$$\boldsymbol{\gamma}^* \equiv \arg \min_{\boldsymbol{\gamma}} \frac{1}{K} \sum_{k=1}^K L(\boldsymbol{\theta}^{(k)}, \hat{\boldsymbol{\theta}}_{\boldsymbol{\gamma}}(\mathbf{Z}^{(k)})), \quad (3)$$

$\{\boldsymbol{\theta}^{(k)} : k = 1, \dots, K\}$ is a set of parameter vectors randomly sampled from $\pi(\boldsymbol{\theta})$ and, independently for each k , $\mathbf{Z}^{(k)}$ are simulated from $f_{\mathbf{Z}|\boldsymbol{\theta}}(\mathbf{z} | \boldsymbol{\theta}^{(k)})$. The process of performing the optimization task (3) on neural-network parameters $\boldsymbol{\gamma}$ defined in (2) is referred to as “training the network”, and this can be performed efficiently using back-propagation and stochastic gradient descent.

The trained neural network $\hat{\boldsymbol{\theta}}_{\boldsymbol{\gamma}^*}(\cdot)$ approximately minimizes the Bayes risk (1), and therefore it is called a *neural Bayes estimator* (NBE). Once trained, an NBE can be applied repeatedly to real data sets at a fraction of the computational cost of conventional inferential methods. It is therefore ideal to use an NBE in settings where inference needs to be made repeatedly; in this case, the initial training cost is said to be amortized over time.

When constructing an NBE, a central consideration in designing the neural-network

architecture, that is, the functional form of (2), is the underlying structure of the data. For example, if the data are gridded, a CNN is typically used (see, e.g., Gerber and Nychka, 2021; Rudi et al., 2021; Lenzi et al., 2023; Richards et al., 2025; Sainsbury-Dale et al., 2024). However, as discussed in Section 1, these standard architectures do not naturally cater for missing data, and this has limited the applicability of neural Bayes estimation. Next, we discuss two approaches that address this challenge.

2.2 The masking approach for missing data

Often, data are incomplete, and one needs to make inference on θ using only a subset of \mathbf{Z} . For a given $\mathbf{Z} \equiv (Z_1, \dots, Z_n)'$, we denote the subvectors of observed and missing elements as \mathbf{Z}_1 and \mathbf{Z}_2 , respectively. We use $\mathcal{I}_1 \equiv \{i : Z_i \text{ is observed}\}$ to denote the ordered set of indices corresponding to the observed component, so that $\mathbf{Z}_1 \equiv (Z_i : i \in \mathcal{I}_1)'$.

The masking approach we present in this section closely follows that of Wang et al. (2024), who applied it in the context of approximate posterior inference. Their approach consists of first constructing a masked version of \mathbf{Z} , denoted by $\mathbf{U} \in \mathcal{U} \subseteq \mathbb{R}^n$, with components

$$\begin{aligned} \mathbf{U}_1 &\equiv (U_i : i \in \mathcal{I}_1)' = \mathbf{Z}_1, \\ \mathbf{U}_2 &\equiv (U_i : i \in \mathcal{I}_2)' = c\mathbf{1}, \end{aligned} \tag{4}$$

where $\mathcal{I}_2 \equiv \{1, \dots, n\} \setminus \mathcal{I}_1$, $c \in \mathbb{R}$ is fixed (we set $c = 0$ throughout), and $\mathbf{1}$ denotes a vector of 1s of appropriate dimension. Then they define a vector of indicator variables, $\mathbf{W} \in \mathcal{W} = \{0, 1\}^n$, as

$$\mathbf{W} \equiv (\mathbb{I}(i \in \mathcal{I}_1) : i = 1, \dots, n)', \tag{5}$$

where $\mathbb{I}(\cdot)$ denotes the indicator function. While \mathbf{Z}_1 and \mathcal{I}_1 have a dimension that might vary across different observed data sets, the quantities \mathbf{U} and \mathbf{W} are each of fixed dimension n , which enables the use of parsimonious, efficient neural-network architectures.

An NBE based on the masking approach is constructed by first defining

$$\hat{\theta}_\gamma(\mathbf{U}, \mathbf{W}) = \mathbf{g}(\mathbf{U}, \mathbf{W}; \gamma), \quad \mathbf{U} \in \mathcal{U}, \mathbf{W} \in \mathcal{W}, \tag{6}$$

where recall $\mathbf{g}(\cdot, \cdot; \gamma)$ is a neural network parameterized by γ , and then substituting

$$\gamma^* \equiv \arg \min_{\gamma} \sum_{k=1}^K L(\theta^{(k)}, \hat{\theta}_\gamma(\mathbf{U}^{(k)}, \mathbf{W}^{(k)})) \tag{7}$$

into (6), where $\theta^{(k)} \sim \pi(\theta)$ and, independently for each k , $\mathbf{U}^{(k)}$ and $\mathbf{W}^{(k)}$ are obtained by sampling indices $\mathcal{I}_1^{(k)}$ from a model $f_{\mathcal{I}_1|\theta}(\mathcal{I}_1 | \theta^{(k)})$ for the missingness mechanism, simulating complete data $\mathbf{Z}^{(k)}$ from the data model $f_{\mathbf{Z}|\theta}(\mathbf{z} | \theta^{(k)})$, subsetting $\mathbf{Z}_1^{(k)} \equiv (Z_i^{(k)} : i \in \mathcal{I}_1^{(k)})'$ and, from these quantities, constructing $\mathbf{U}^{(k)}$ and $\mathbf{W}^{(k)}$ using (4) and (5), respectively. Once trained, the neural network can be used repeatedly to estimate parameters from new incomplete data sets. Algorithm 1 summarizes the approach, and Figure 1 illustrates its estimation stage.

Algorithm 1 The masking approach to neural Bayes estimation with missing data.

Training stage (slow, to be done only once offline)

Require: Prior $\pi(\boldsymbol{\theta})$, number of training samples K , probability models $f_{\mathcal{I}_1|\boldsymbol{\theta}}(\mathcal{I}_1 | \boldsymbol{\theta})$ and $f_{\mathbf{Z}|\boldsymbol{\theta}}(\mathbf{z} | \boldsymbol{\theta})$, $c \in \mathbb{R}$ for use in (4), loss function $L(\cdot, \cdot)$, neural network $\hat{\boldsymbol{\theta}}_\gamma(\cdot, \cdot)$ of the form (6).

- 1: **for** $k = 1, \dots, K$ **do**
- 2: Sample parameters $\boldsymbol{\theta}^{(k)} \sim \pi(\boldsymbol{\theta})$.
- 3: Sample indices $\mathcal{I}_1^{(k)} \sim f_{\mathcal{I}_1|\boldsymbol{\theta}}(\mathcal{I}_1 | \boldsymbol{\theta}^{(k)})$.
- 4: Simulate data $\mathbf{Z}^{(k)} \sim f_{\mathbf{Z}|\boldsymbol{\theta}}(\mathbf{z} | \boldsymbol{\theta}^{(k)})$.
- 5: Subset $\mathbf{Z}_1^{(k)} \equiv (\mathbf{Z}_i^{(k)} : i \in \mathcal{I}_1^{(k)})'$.
- 6: Compute $\mathbf{U}^{(k)}$ using (4).
- 7: Compute $\mathbf{W}^{(k)}$ using (5).
- 8: **end for**
- 9: Solve $\gamma^* \equiv \operatorname{argmin}_\gamma \sum_{k=1}^K L(\boldsymbol{\theta}^{(k)}, \hat{\boldsymbol{\theta}}_\gamma(\mathbf{U}^{(k)}, \mathbf{W}^{(k)}))$.
- 10: Substitute γ^* into (6) to obtain the masked NBE, $\hat{\boldsymbol{\theta}}_{\gamma^*}(\cdot, \cdot)$.

Estimation stage (fast, repeatable for arbitrarily many observed data sets)

Require: Observed data \mathbf{Z}_1 and \mathcal{I}_1 , $c \in \mathbb{R}$ for use in (4).

- 1: Compute \mathbf{U} using (4).
 - 2: Compute \mathbf{W} using (5).
 - 3: Return $\hat{\boldsymbol{\theta}}_{\gamma^*}(\mathbf{U}, \mathbf{W})$.
-

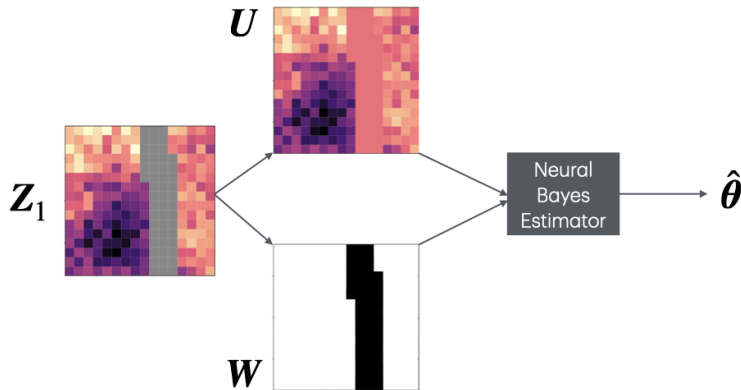


Figure 1: The estimation stage of Algorithm 1. Observed data \mathbf{Z}_1 , and the associated indices \mathcal{I}_1 (here, implicit) that identify which elements of \mathbf{Z} are observed, are used to construct \mathbf{U} , a masked version of the complete data \mathbf{Z} with missing entries replaced by a constant $c \in \mathbb{R}$, and \mathbf{W} , a vector of indicator variables that encode the missingness pattern. The encoded data \mathbf{U} and \mathbf{W} are then input to an NBE to obtain point estimates $\hat{\boldsymbol{\theta}}$ of a model parameter $\boldsymbol{\theta}$.

Algorithm 1 has a number of strengths. It does not place any restriction on the loss function and it only requires simulation from $f_{\mathcal{I}_1|\boldsymbol{\theta}}(\mathcal{I}_1 | \boldsymbol{\theta})$ and $f_{\mathbf{Z}|\boldsymbol{\theta}}(\mathbf{z} | \boldsymbol{\theta})$. Further, no information on $\boldsymbol{\theta}$ is lost by using \mathbf{U} and \mathbf{W} instead of \mathbf{Z}_1 and \mathcal{I}_1 , since there is a one-to-one mapping between these quantities (see Theorem 1 in Section S1 of the Supplementary

Material). However, the approach has two drawbacks. First, the neural network must learn a mapping from $\mathcal{U} \times \mathcal{W}$ to Θ . This learning task can be more challenging than learning a mapping from \mathcal{Z} to Θ , since an element in $\mathcal{U} \times \mathcal{W}$ is semi-discrete and of dimension $2n$. Second, when treating \mathbf{U} and \mathbf{W} as the data, the Bayes risk (1) of the estimator $\hat{\boldsymbol{\theta}}(\cdot, \cdot)$ becomes

$$r(\hat{\boldsymbol{\theta}}(\cdot, \cdot)) \equiv \sum_{\mathbf{w} \in \mathcal{W}} \int_{\Theta} \int_{\mathcal{U}} L(\boldsymbol{\theta}, \hat{\boldsymbol{\theta}}(\mathbf{u}, \mathbf{w})) f_{\mathbf{U}, \mathbf{W} | \boldsymbol{\theta}}(\mathbf{u}, \mathbf{w} | \boldsymbol{\theta}) \pi(\boldsymbol{\theta}) d\mathbf{u} d\boldsymbol{\theta}. \quad (8)$$

It is a corollary of Theorem 1 in Section S1 of the Supplementary Material and Bayesian sufficiency (e.g., Cox and Hinkley, 1974, Ch. 2) that a Bayes estimator that minimizes (8) also minimizes the Bayes risk defined in terms of \mathbf{Z}_1 and \mathcal{I}_1 . Further, under the assumption that \mathcal{I}_1 is independent of $\boldsymbol{\theta}$, which is often reasonable in practice, it follows from Richards et al. (2025, Theorem 1) and Sainsbury-Dale et al. (2025, Theorem 1) that a Bayes estimator that minimizes (8) is invariant to distributions on \mathcal{I}_1 that are positive everywhere. However, in practice, the empirical analogue of (8), given in (7), is subject to Monte Carlo error that depends on the chosen distribution for \mathcal{I}_1 . Therefore, the choice of distribution has practical implications on the approximation of the Bayes estimator obtained by substituting (7) into (6), particularly in high-dimensional settings where the total number of possible missingness patterns (2^n) is large and the missingness mechanism is difficult to specify. In Section 3, we show through simulation that selecting a distribution for \mathcal{I}_1 that assigns low probability to the observed missingness pattern can lead to statistically inefficient estimators.

To address these limitations, we propose an alternative statistical approach to neural Bayes estimation with incomplete data. Our approach does not require the missingness pattern to be an input to the neural network, or the specification of a missingness mechanism. We do this by embedding neural networks in a classical data-augmentation approach to solving incomplete-data problems, namely a Monte Carlo EM algorithm.

2.3 The EM approach for missing data

In Section 2.3.1, we provide an overview of the classical EM algorithm and its Monte Carlo version. In Section 2.3.2, we outline the general structure of our proposed EM approach to neural Bayes estimation with incomplete data. In Section 2.3.3, we detail the construction of a neural approximation to the MAP estimator, which is needed for our EM approach.

2.3.1 The classical EM algorithm and its Monte Carlo version

Recall that we use \mathbf{Z}_1 and \mathbf{Z}_2 to denote the subvectors of \mathbf{Z} that are treated as observed and missing, respectively, and that we use \mathbf{Z} to denote the complete data. We also have available an ordered set of indices, \mathcal{I}_1 , associated with \mathbf{Z}_1 . However, since one does not need to construct a mask from these indices in our approach described below, we omit the explicit notation of these indices in this subsection.

In the classical statistics literature, many algorithms have been developed based on the “data augmentation principle,” which is applied when inference based on \mathbf{Z} is easier than inference based only on \mathbf{Z}_1 (see, e.g., Tanner and Wong, 1987; Gelfand and Smith, 1990; van Dyk and Meng, 2001; Tanner and Wong, 2010). A popular approach to point estimation that follows from this principle is the EM algorithm (Dempster et al., 1977; Wu, 1983; McLachlan

and Krishnan, 2007), an iterative algorithm for estimating $\boldsymbol{\theta}$ with the l th iteration given by

$$\hat{\boldsymbol{\theta}}^{(l)} = \arg \max_{\boldsymbol{\theta}} \mathbb{E}_{\mathbf{Z}_2 | \mathbf{Z}_1, \hat{\boldsymbol{\theta}}^{(l-1)}} \ell(\boldsymbol{\theta}; \mathbf{Z}_1, \mathbf{Z}_2); \quad l = 1, 2, \dots, \quad (9)$$

where $\ell(\boldsymbol{\theta}; \mathbf{Z}_1, \mathbf{Z}_2) \equiv \log f_{\mathbf{Z} | \boldsymbol{\theta}}(\mathbf{Z} | \boldsymbol{\theta})$ denotes the complete-data log-likelihood. The EM algorithm increases the incomplete-data log-likelihood, $\log f_{\mathbf{Z}_1 | \boldsymbol{\theta}}(\mathbf{Z}_1 | \boldsymbol{\theta})$, at each iteration and, thus, under mild conditions (see, e.g., Boyles, 1983; Wu, 1983), it yields a local maximizer of the incomplete-data log-likelihood.

When the conditional expectation in (9) is intractable but conditional simulation is feasible, one often adopts a Monte Carlo version of the EM algorithm (Wei and Tanner, 1990; Ruth, 2024), which has as the l th iteration,

$$\hat{\boldsymbol{\theta}}^{(l)} = \arg \max_{\boldsymbol{\theta}} \frac{1}{H} \sum_{h=1}^H \ell(\boldsymbol{\theta}; \mathbf{Z}_1, \mathbf{Z}_2^{(l,h)}), \quad (10)$$

where $\{\mathbf{Z}_2^{(l,h)} : h = 1, \dots, H\}$ are simulated from the distribution of $\mathbf{Z}_2 | \mathbf{Z}_1, \hat{\boldsymbol{\theta}}^{(l-1)}$. For discussion on the properties of the Monte Carlo EM algorithm, see Chan and Ledolter (1995), Fort and Moulines (2003), and Neath (2013, Sec. 4).

In a Bayesian setting, one may replace the log-likelihood term in (9) with $\ell(\boldsymbol{\theta}; \mathbf{Z}_1, \mathbf{Z}_2) + \log \pi(\boldsymbol{\theta})$, where $\pi(\cdot)$ denotes a given prior density of $\boldsymbol{\theta}$, in which case the EM algorithm yields a local maximizer of the posterior density of $\boldsymbol{\theta} | \mathbf{Z}_1$, that is, a local MAP estimate (Dempster et al., 1977). Similarly, a Bayesian version of the Monte Carlo EM algorithm has as the l th iteration,

$$\hat{\boldsymbol{\theta}}^{(l)} = \arg \max_{\boldsymbol{\theta}} \frac{1}{H} \sum_{h=1}^H \ell(\boldsymbol{\theta}; \mathbf{Z}_1, \mathbf{Z}_2^{(l,h)}) + \log \pi(\boldsymbol{\theta}). \quad (11)$$

In this paper, we focus on the algorithm defined by (11).

A drawback of the (Monte Carlo) EM algorithm is that it can be slow since it is “doubly iterative” in the typical case that each maximization step requires numerical optimization. A substantial amount of work has been devoted to trying to speed up the algorithm, primarily by accelerating its rate of convergence (e.g., Louis, 1982; Meng and Rubin, 1993; Liu and Rubin, 1994; Jamshidian and Jennrich, 1997; Neal and Hinton, 1998; Varadhan and Roland, 2008). Further, although the Monte Carlo EM algorithm bypasses the conditional expectation in (9), it still requires evaluation of the complete-data log-likelihood function, which is not always possible. Next, we describe how the Monte Carlo EM algorithm can facilitate the use of NBEs with incomplete data in a manner that is not subject to these limitations.

2.3.2 NBEs and the Monte Carlo EM algorithm

Our EM approach for using NBEs with incomplete data is predicated on the fact that (11) is equivalent to,

$$\hat{\boldsymbol{\theta}}^{(l)} = \arg \max_{\boldsymbol{\theta}} \sum_{h=1}^H \ell(\boldsymbol{\theta}; \mathbf{Z}_1, \mathbf{Z}_2^{(l,h)}) + \log \pi_H(\boldsymbol{\theta}), \quad (12)$$

Algorithm 2 The EM approach to neural Bayes estimation with missing data.

Training stage (slow, to be done only once offline)

Require: Prior $\pi(\boldsymbol{\theta})$, number of training samples K , number of Monte Carlo samples H used in the inference stage, probability model $f_{\mathbf{Z}|\boldsymbol{\theta}}(\mathbf{z} | \boldsymbol{\theta})$, neural network $\hat{\boldsymbol{\theta}}_{\gamma}(\cdot)$ of the form (15) that takes as input a set of replicates $\{\mathbf{Z}^{(h)} \in \mathcal{Z}\}_{h=1}^H$.

- 1: **for** $k = 1, \dots, K$ **do**
- 2: Sample parameters $\boldsymbol{\theta}^{(k)} \sim \pi_H(\boldsymbol{\theta})$ where $\pi_H(\boldsymbol{\theta}) \propto \{\pi(\boldsymbol{\theta})\}^H$.
- 3: Simulate data $\mathbf{Z}^{(k,h)} \sim f_{\mathbf{Z}|\boldsymbol{\theta}}(\mathbf{z} | \boldsymbol{\theta}^{(k)})$ for $h = 1, \dots, H$.
- 4: **end for**
- 5: Solve $\gamma^* \equiv \operatorname{argmin}_{\gamma} \sum_{k=1}^K L(\boldsymbol{\theta}^{(k)}, \hat{\boldsymbol{\theta}}_{\gamma}(\{\mathbf{Z}^{(k,h)}\}_{h=1}^H))$ with $L(\cdot, \cdot)$ a continuous and almost-everywhere differentiable approximation to the 0–1 loss function (e.g., (14)).
- 6: Substitute γ^* into (15) to obtain the NBE, $\hat{\boldsymbol{\theta}}_{\gamma^*}(\cdot)$, that approximates the MAP estimator.

Estimation stage (fast, repeatable for arbitrarily many observed data sets)

Require: Observed data \mathbf{Z}_1 , number of Monte Carlo samples H , initial estimates $\hat{\boldsymbol{\theta}}^{(0)}$, convergence criterion, maximum number of iterations M , ability to simulate from the conditional distribution of $\mathbf{Z}_2 | \mathbf{Z}_1, \boldsymbol{\theta}$.

- 1: Set $l = 0$.
 - 2: **while** not converged and $l < M$ **do**
 - 3: Set $l = l + 1$.
 - 4: Simulate missing data $\mathbf{Z}_2^{(l,h)} \sim \mathbf{Z}_2 | \mathbf{Z}_1, \hat{\boldsymbol{\theta}}^{(l-1)}$, $h = 1, \dots, H$, conditional on observed incomplete data and current parameter estimates. Each simulated data vector is concatenated with \mathbf{Z}_1 fixed, resulting in H conditionally independent replicates of the completed data, $\{\mathbf{Z}^{(l,h)}\}_{h=1}^H$.
 - 5: Perform the update (12) by computing $\hat{\boldsymbol{\theta}}^{(l)} = \hat{\boldsymbol{\theta}}_{\gamma^*}(\{\mathbf{Z}^{(l,h)}\}_{h=1}^H)$.
 - 6: **end while**
 - 7: Return $\hat{\boldsymbol{\theta}}^{(l)}$.
-

where $\pi_H(\boldsymbol{\theta}) \propto \{\pi(\boldsymbol{\theta})\}^H$. The update (12) is a MAP estimate that may be approximated by a suitably constructed NBE (see Section 2.3.3 for details). This leads to our proposed EM approach (Algorithm 2), which is a fast version of the Monte Carlo EM algorithm that does not require the evaluation of any likelihood functions. Figure 2 illustrates the estimation stage of the algorithm. Rather than focusing on the rate of convergence, our approach decreases the total run-time of the Monte Carlo EM algorithm by speeding up each iteration; after conditional simulation, the update (12) is obtained in a fraction of a second. Importantly, since the incomplete data are completed by conditional simulation, the NBE is applied to complete-data vectors only and, therefore, our proposed algorithm does not require a model for the missingness mechanism.

Our EM approach is applicable when simulations can be carried out from the distributions of $\mathbf{Z} | \boldsymbol{\theta}$ and $\mathbf{Z}_2 | \mathbf{Z}_1, \boldsymbol{\theta}$, and it is an obvious approach to try when the incomplete-data and complete-data likelihoods are intractable. Statistical models that satisfy these conditions are (hidden) Markov random fields (e.g., Besag, 1974; Rue and Held, 2005). Notable examples are the Potts (1952) model considered in Section 3.3, the autologistic model (Besag, 1972),

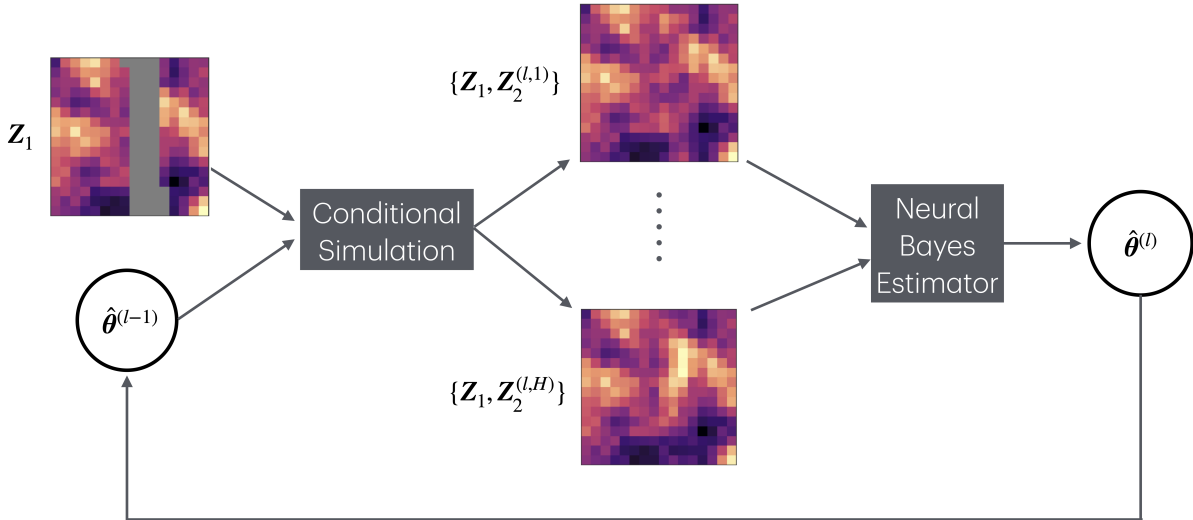


Figure 2: The estimation stage of Algorithm 2. Incomplete data Z_1 with missing entries are completed by conditional simulation using the previous parameter estimate $\hat{\theta}^{(l-1)}$ of model parameter θ . The conditionally-independent replicates are then input to an NBE trained to approximate the MAP estimator under the prior $\pi_H(\theta) \propto \{\pi(\theta)\}^H$. The parameter estimate $\hat{\theta}^{(l)}$ is then used for conditional simulation in the next iteration of the algorithm.

and other auto-models proposed by Besag (1974). These models have intractable likelihoods due to the computational complexity of the required normalizing constants. However, marginal and conditional simulation is feasible through Gibbs sampling.

The considerations regarding the choice of H and the EM convergence criterion apply equally to both the conventional Monte Carlo EM algorithm and Algorithm 2. For instance, to avoid wasting computational effort in the early stages of the algorithm, H is often chosen adaptively across iterations. This adaptation is typically based on the Monte Carlo error at each iteration, evaluated under the asymptotic behaviour of the log-likelihood function (e.g., Chan and Ledolter, 1995; Booth and Hobert, 1999; Levine and Casella, 2001; Caffo et al., 2005). However, since Algorithm 2 does not provide log-likelihood information, one may instead fix H to some moderately large value or increase it at predetermined iterations (as done by, e.g., Wei and Tanner, 1990; McCulloch, 1997). With regard to assessing convergence, we follow Booth and Hobert (1999) and stop the algorithm if the relative change in parameter values is smaller than a specified tolerance for three successive iterations. Details on our specific choices for H and the convergence criterion are provided in Section 3.1.

2.3.3 Neural MAP estimation

Algorithm 2 hinges on the capacity to approximate the MAP estimator using an NBE. Here, we outline how this can be done. For continuous parameter spaces, the MAP estimator is

the limit as $\epsilon \rightarrow 0$ of the Bayes estimators associated with the 0–1 loss function

$$L(\boldsymbol{\theta}, \hat{\boldsymbol{\theta}}) = \mathbb{I}(\|\boldsymbol{\theta} - \hat{\boldsymbol{\theta}}\| > \epsilon), \quad (13)$$

where $\|\cdot\|$ denotes any norm in \mathbb{R}^p (Robert, 2007, pg. 166). The construction of an NBE that approximates the MAP estimator for use in (12) is therefore possible in principle, but several practical challenges must be overcome.

First, the loss function (13) is not amenable to gradient-based methods for solving (3). This challenge may be circumvented by noting that, under suitable regularity conditions, for large H and uniform prior $\pi(\boldsymbol{\theta})$, the objective in (12) tends to the logarithm of an unnormalised Gaussian density (Bernstein–von Mises theorem; see, e.g., van der Vaart, 1998, pg. 140). Since the mean of a Gaussian random variable is also its mode, one could choose a quadratic loss function instead of (13). Alternatively, one may adopt a mathematically convenient surrogate for (13) with derivatives that are continuous almost everywhere, as we do here. For example,

$$L(\boldsymbol{\theta}, \hat{\boldsymbol{\theta}}; \kappa) \equiv \tanh(\|\hat{\boldsymbol{\theta}} - \boldsymbol{\theta}\|/\kappa), \quad \kappa > 0, \quad (14)$$

where $\tanh(\cdot)$ denotes the hyperbolic tangent function, yields the 0–1 loss function in the limit as $\kappa \rightarrow 0$ (see Section S2 of the Supplementary Material). Therefore, instead of (13) for some ϵ close to 0, we use (14) for some κ close to 0.

Our second challenge is due to the update (12) being computed under a concentrated prior density, $\pi_H(\boldsymbol{\theta}) \propto \{\pi(\boldsymbol{\theta})\}^H$, which needs to be easily sampled from (see Algorithm 2). A natural solution is to choose $\pi(\boldsymbol{\theta})$ such that $\pi_H(\boldsymbol{\theta})$ is amenable to sampling. If the elements of $\boldsymbol{\theta}$ are assumed to be independent a priori, convenient choices for the marginal priors include the uniform, beta, (truncated) Gaussian, Pareto, and gamma distributions, since these families are closed under power transformations of their density functions. The uniform distribution is particularly convenient since, after normalization, it is invariant to power transformations of its density function. For subsets of parameters that are dependent a priori, one might similarly choose a family of multivariate distributions that are closed under power transformations of their density functions, such as the multivariate Gaussian, Dirichlet, and LKJ (Lewandowski et al., 2009) distributions.

Finally, in Algorithm 2, (12) involves neural Bayes estimation from replicated data. This can be implemented using the DeepSets framework (Zaheer et al., 2017), with the neural network $\mathbf{g}(\cdot; \boldsymbol{\gamma})$ expressed in the form:

$$\hat{\boldsymbol{\theta}}_{\boldsymbol{\gamma}}(\{\mathbf{Z}^{(h)}\}_{h=1}^H) = \mathbf{g}(\{\mathbf{Z}^{(h)}\}_{h=1}^H; \boldsymbol{\gamma}) = \boldsymbol{\phi}\left(\frac{1}{H} \sum_{h=1}^H \boldsymbol{\psi}(\mathbf{Z}^{(h)}; \boldsymbol{\gamma}_{\psi}); \boldsymbol{\gamma}_{\phi}\right), \quad (15)$$

where $\mathbf{Z}^{(h)} \in \mathcal{Z}$, $h = 1, \dots, H$, $\boldsymbol{\psi}(\cdot; \boldsymbol{\gamma}_{\psi})$ is a neural network whose architecture depends on the structure of the data (e.g., a CNN for gridded data), $\boldsymbol{\phi}(\cdot; \boldsymbol{\gamma}_{\phi})$ is a multilayer perceptron, and the neural-network parameters are $\boldsymbol{\gamma} = (\boldsymbol{\gamma}'_{\psi}, \boldsymbol{\gamma}'_{\phi})'$. The representation (15) has several motivations. First, Bayes estimators for conditionally independent data (when conditional on $\boldsymbol{\theta}$) are permutation invariant, and estimators constructed from (15) are guaranteed to exhibit this property. Second, (15) is a universal approximator for continuously differentiable

permutation-invariant functions (e.g., Wagstaff et al., 2022); therefore, any Bayes estimator that is a continuously differentiable function of the data can be approximated arbitrarily well by an estimator of the form (15). Third, (15) may be used with any value of H . See Sainsbury-Dale et al. (2024) for further details on the use of (15) in the context of neural Bayes estimation and a discussion of the architecture’s connection to conventional estimators. For an illustration of neural MAP estimation with a simple model, see Figures S9 and S10 of the Supplementary Material.

3 Simulation studies

We now conduct simulation studies to investigate the strengths and weaknesses of the masking approach (Algorithm 1) compared to our EM approach (Algorithm 2), both developed for estimation in the presence of missing data. We refer to an NBE employing the masking approach as a “Masking NBE”, and an NBE employing our EM approach as an “EM NBE”. In Section 3.1, we outline the general setting. In Section 3.2, we assume a spatial Gaussian-process model and estimate its parameters. Since the likelihood function is available for this model, we compare the two competing NBEs to the MAP estimator that (numerically) maximizes the posterior density. In Section 3.3, we consider the Potts (1952) model, which is a Markov-random-field model for discrete categorical data. In contrast to Section 3.2, the likelihood function here involves a computationally intractable normalizing constant, and hence likelihood-free methods are an obvious inferential choice.

3.1 General setting

We conduct our experiments using functionality we have added to the package **NeuralEstimators** (Sainsbury-Dale, 2024), which is available in Julia and R. We use a workstation with an AMD EPYC 7402 3.00GHz CPU with 128 GB of CPU RAM, and a Nvidia Quadro RTX 6000 GPU with 24 GB of GPU RAM. All subsequent results can be generated using reproducible code at <https://github.com/msainsburydale/NeuralIncompleteData>.

To elucidate the differences between the masking approach (Algorithm 1) and the EM approach (Algorithm 2), which are greater with data that are high-dimensional, our simulation studies consider spatial models where the data are observed incompletely over a regular grid of size $n = 64^2 = 4096$, and we therefore use a CNN-based architecture for (2) and (6) detailed in Section S3 of the Supplementary Material. There, we also illustrate the benefits of using an ensemble (Hansen and Salamon, 1990; Breiman, 1996) of neural networks in the context of neural Bayes estimation; throughout our experiments we use an ensemble of five NBEs for both the masking and EM approaches. Although here our grid is fixed, our chosen architecture can accommodate data sets collected over grids of varying size and shape; see Section S4 of the Supplementary Material.

We train our NBEs under the loss function (14), with $\kappa = 0.1$ and $K = 25000$ in both (3) (EM) and (7) (Masking). We cease training when the objective function in (3) or (7) has not decreased in five consecutive epochs, where an epoch is defined to be one complete pass through the entire training data set when doing stochastic gradient descent to decrease the objective functions. When training the Masking NBEs, we use a missing completely at

Table 1: The neural-network training time, estimation time for a single test data set, and empirical RMSE under two missingness models for three estimators of the parameters of the Gaussian process model (Section 3.2). The missingness models for these test data are missing completely at random (MCAR) and missing in a contiguous block (MICB). Empirical RMSEs are based on 1000 simulated data sets.

Estimator	Training time (mins)	Estimation time (s)	RMSE _{MCAR}	RMSE _{MICB}
MAP	–	1.12	0.021	0.022
EM NBE	21.6	0.39	0.021	0.022
Masking NBE	25.3	0.01	0.022	0.157

random (MCAR) model for the missingness mechanism, with the percentage of missing data varying uniformly between 10% and 90% across data sets.

Following training, the estimators’ statistical efficiencies are compared on previously unseen test data under both MCAR missingness and a model for the missingness where data are missing in a contiguous block (MICB), with the proportion of missing data fixed to 20%. This is done to assess the Masking NBEs under the correct and an incorrect specification of the missingness mechanism. For the EM NBEs, we set $H = 30$ in (12); we use the mean of the prior distribution (as defined in Sections 3.2 and 3.3) for the initial estimates, $\hat{\boldsymbol{\theta}}^{(0)}$; and we stop the algorithm after 50 iterations or if $\max(\{|\hat{\theta}_q^{(l+1)} - \hat{\theta}_q^{(l)}|/|\hat{\theta}_q^{(l)}| : q = 1, \dots, p\}) < 0.01$ for three consecutive values of l .

3.2 Gaussian process model

In this simulation study, we consider a spatial Gaussian process model, where $\mathbf{Z} \equiv (Z_1, \dots, Z_n)'$ are data at locations $\{\mathbf{s}_1, \dots, \mathbf{s}_n\}$ in a spatial domain $\mathcal{D} \subseteq \mathbb{R}^2$. The data are modeled as spatially-correlated mean-zero Gaussian random variables with Matérn covariance function, given by

$$\text{cov}(Z_i, Z_j) = \sigma^2 \frac{2^{1-\nu}}{\Gamma(\nu)} \left(\frac{\|\mathbf{s}_i - \mathbf{s}_j\|}{\rho} \right)^\nu K_\nu \left(\frac{\|\mathbf{s}_i - \mathbf{s}_j\|}{\rho} \right) + \tau^2 \mathbb{I}(i = j), \quad i, j = 1, \dots, n, \quad (16)$$

where σ^2 is a variance parameter, $\Gamma(\cdot)$ is the gamma function, $K_\nu(\cdot)$ is the modified Bessel function of the second kind of order ν , $\rho > 0$ and $\nu > 0$ are range and smoothness parameters, respectively, and τ^2 is a fine-scale variance parameter.

In this example, we take the spatial domain to be $\mathcal{D} \equiv [0, 1] \times [0, 1]$, and we simulate complete data on a regular square grid of size $n = 64^2 = 4096$. For computational tractability, we use the package **GpGp** to simulate training data via the Vecchia (1988) approximation. We implement the Vecchia approximation using a maxmin ordering of the locations, with a maximum of 30 neighbors assigned to each location; see Guinness (2018) for further details. The parameters to be estimated are $\boldsymbol{\theta} \equiv (\tau, \rho)'$, and we fix $\nu = 1$ and $\sigma^2 = 1$. We assume that τ and ρ are independent a priori, and we use the priors $\tau \sim \text{Unif}(0, 1)$ and $\rho \sim \text{Unif}(0, 0.35)$.

We compare the estimators using the neural-network training times, estimation times for a single data set post-training (computational efficiency), and empirical root-mean-squared errors (RMSEs) (statistical efficiency) based on simulated data using 1000 parameter vectors

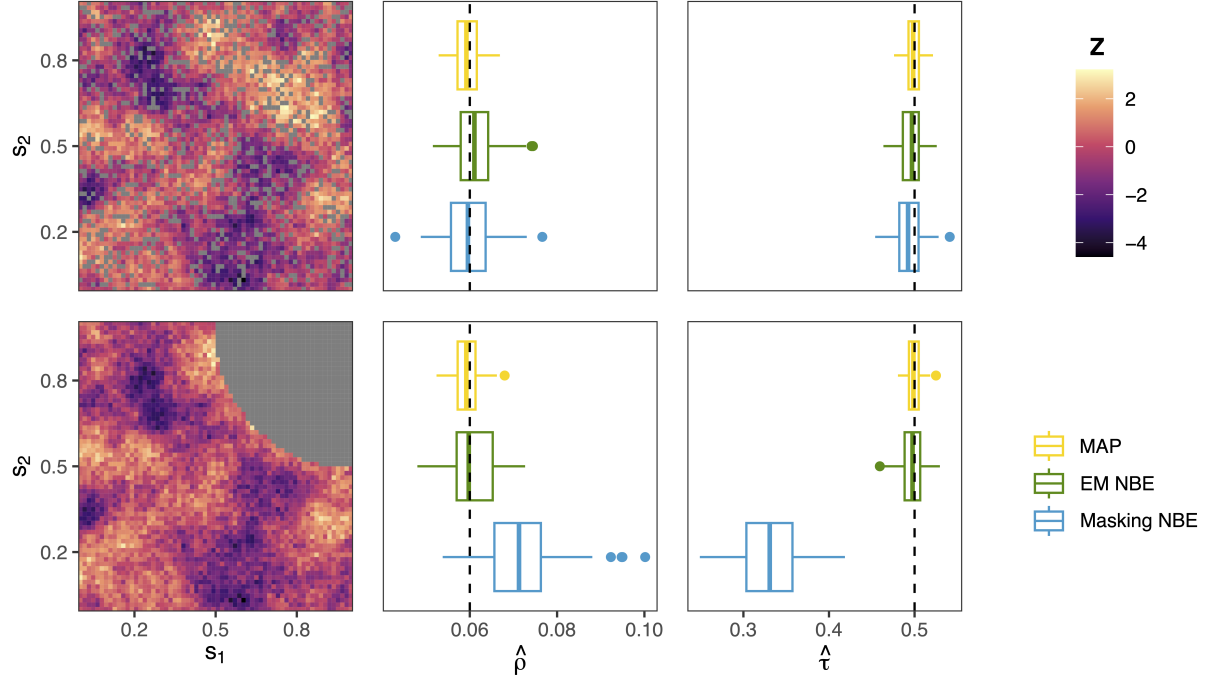


Figure 3: Spatial data (first column) where the missingness is of type MCAR (first row) or MICB (second row) with missingness shown in gray, and corresponding empirical distributions (second and third columns) for three estimators of the parameters of the Gaussian process model (Section 3.2). The boxplots are staggered for easy vertical assessment. True parameter values are shown as a dashed vertical line.

sampled from the prior. For the 1000 parameter vectors $\{\theta^{(1)}, \dots, \theta^{(1000)}\}$ and an estimator $\hat{\theta}(\cdot)$,

$$\text{RMSE}(\hat{\theta}(\cdot)) = \left\{ \frac{1}{1000} \sum_{j=1}^{1000} \|\hat{\theta}^{(j)} - \theta^{(j)}\|^2 \right\}^{1/2}, \quad (17)$$

where, for $j = 1, \dots, 1000$, $\hat{\theta}^{(j)}$ is the corresponding estimate from incomplete data $\mathbf{Z}_1^{(j)} \sim f_{\mathbf{Z}_1|\theta}(\mathbf{z}_1 | \theta^{(j)})$, and $\|\cdot\|$ denotes the Euclidean norm. We use $\text{RMSE}_{\text{MCAR}}$ and $\text{RMSE}_{\text{MICB}}$ to denote the RMSE of an estimator based on incomplete data simulated under the MCAR and MICB mechanisms, respectively, where missingness is independent of the parameter vector. Table 1 summarizes the results, while Figure 3 shows simulated data and corresponding boxplots of the empirical distributions of the estimates for one parameter setting. Our results highlight several important properties of the two NBEs.

First, the EM NBE is agnostic to the missingness pattern and it performs well under both MCAR and MICB data, as illustrated by the similarity of the EM NBE’s sampling distribution (Figure 3) and RMSE (Table 1) to those of the MAP estimator. In contrast, the Masking NBE takes as input the missingness pattern, which can complicate the learning task, and it necessitates a model for the missingness pattern when generating training data. As discussed in Section 2.2, this can lead to bias when the missingness model is misspecified, which is likely to occur in practice. In our simulation study, we do indeed observe a large

RMSE (Table 1) and bias (Figure 3) for MICB test data (recall that the Masking NBE was trained with MCAR data).

Second, the estimators represent a trade-off between computational efficiency and statistical efficiency, particularly for a misspecified missingness mechanism. The speed of the Masking NBE is due to its not requiring likelihood computation or conditional simulation, and because it is not an iterative algorithm. For the spatial Gaussian process model, the MAP estimate is obtained straightforwardly by numerically maximizing the unnormalized posterior density, which here is available in closed form. Hence, for this model, the EM NBE provides only a moderate reduction in estimation time compared to the MAP estimator (Table 1).

These results provide empirical evidence that neural-network, likelihood-free approaches can be almost as statistically efficient as a gold-standard likelihood-based estimator. It will be seen in the next section that NBEs are even more beneficial when the incomplete data likelihood function is unavailable in closed form or computationally intractable.

3.3 Potts model

We now consider a Markov random field (e.g., Besag, 1974; Cressie, 1993, Ch. 6; Rue and Held, 2005), specifically the Potts (1952) model. The Potts model has been used extensively in statistical image analysis (e.g., Marin and Robert, 2007, Ch. 8; Vu et al., 2021), in the analysis of spatial extremes (Reich and Shaby, 2018), and in statistical physics (e.g., Onsager, 1944; Chen et al., 2021). Here, we focus on its formulation in a spatial-random-field context. Specifically, consider a regular grid of pixels indexed by $i = 1, \dots, n$, where each pixel takes on a value Z_i from a finite set of discrete states $\mathcal{Q} \equiv \{1, \dots, Q\}$. Then, the Potts model is specified through the conditional distributions,

$$\Pr(Z_i = z \mid \mathbf{Z}_{\setminus i}, \beta) \propto \exp \left\{ \beta \sum_{j \in \mathcal{N}_i} \mathbb{I}(Z_j = z) \right\}, \text{ for } z \in \mathcal{Q}, \quad (18)$$

where $\mathbf{Z}_{\setminus i}$ denotes all pixel labels excluding the i th pixel; $\beta > 0$ is a parameter controlling the strength of spatial dependence; and \mathcal{N}_i contains the indices of the “neighbors” of pixel i . Here, we consider a Potts model modified to account for edge effects. Specifically, we let the neighbors \mathcal{N}_i be the adjacent pixels of pixel i , with four neighbors for interior pixels, three for edge pixels, and two for corner pixels. The Potts model exhibits a phase transition at the critical parameter value $\beta_c = \log(1 + \sqrt{Q})$ (Moores et al., 2021), transitioning from disorder when $\beta < \beta_c$ (where most neighboring pixels do not have the same label) to order when $\beta > \beta_c$ (where most neighboring pixels have the same label). In spatial statistics, it is known as an auto-model (Besag, 1972), and its likelihood function can be written as

$$\Pr(\mathbf{Z} = \mathbf{z} \mid \beta) = \exp \{ \beta S(\mathbf{z}) \} / C(\beta), \quad \mathbf{z} \in \mathcal{Q}^n, \quad (19)$$

where the sufficient statistic $S(\mathbf{z}) \equiv \sum_{i=1}^n \sum_{j \in \mathcal{N}_i} \mathbb{I}(z_j = z_i)$ contains the total number of neighboring pixels with the same label, and $C(\beta) \equiv \sum_{\mathbf{q} \in \mathcal{Q}^n} \exp \{ \beta S(\mathbf{q}) \}$ is a normalizing constant involving a sum over all possible label combinations, which requires $\mathcal{O}(Q^n)$ operations to evaluate. Due to the intractability of the normalizing constant for large n ,

Table 2: The neural-network training time, estimation time for a single test data set, and empirical RMSE for two estimators of the Potts Model’s parameter (Section 3.3). The missingness mechanisms for these test data are MCAR and MICB. Empirical RMSEs are based on 1000 simulated data sets.

Estimator	Training time (mins)	Estimation time (s)	RMSE _{MCAR}	RMSE _{MICB}
EM NBE	37.3	0.09	0.032	0.031
Masking NBE	72.1	0.01	0.035	0.097

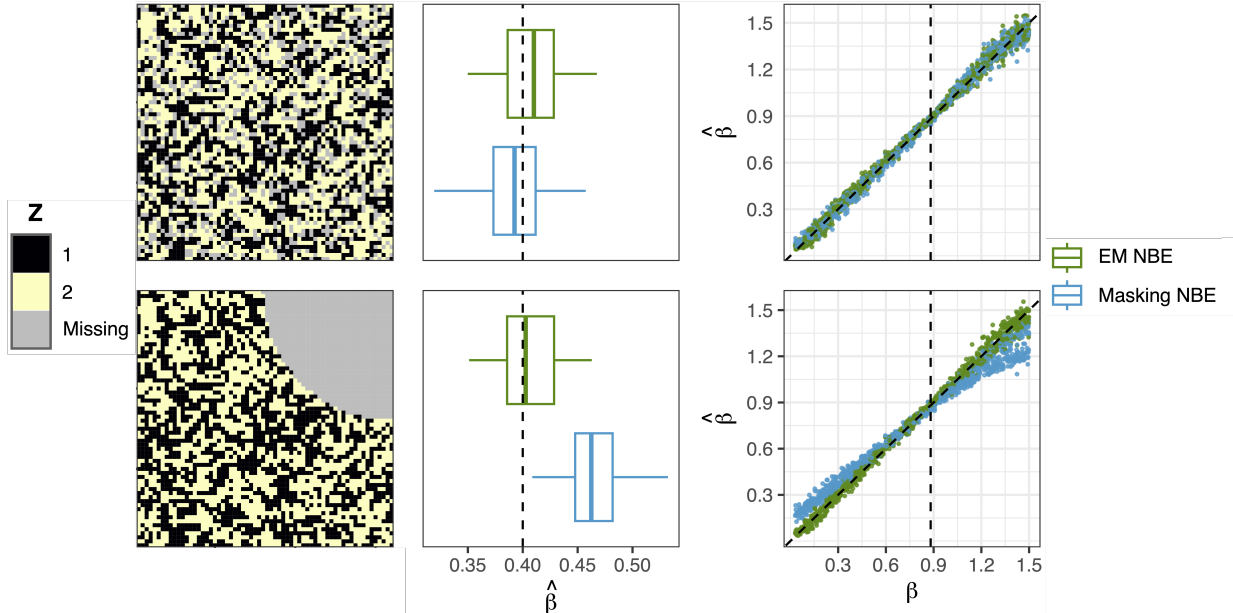


Figure 4: Spatial data (first column) where the missingness is of type MCAR (first row) or MICB (second row), empirical distributions (second column) for $\beta = 0.4$ (dashed vertical line), and estimates versus true values (third column; critical parameter value $\beta_c \approx 0.881$ demarcated by dashed vertical line) for many different parameter values, for two estimators of the Potts Model’s parameter of Section 3.3.

likelihood-based inference is infeasible for the Potts model with even moderately-sized grids.

In this example, we consider the Potts model with $Q = 2$ states, a special case known as the [Ising \(1925\)](#) model. Here, the phase transition occurs at $\beta_c \approx 0.881$. We adopt the prior $\beta \sim \text{Unif}(0, 1.5)$, and we estimate β based on incomplete data on a square grid of size $n = 64^2 = 4096$. To simulate realizations of the complete-data vector \mathbf{Z} during the training stages of Algorithms 1 and 2, we employ the [Swendsen and Wang \(1987\)](#) algorithm implemented in the package [bayesImagesS \(Moore et al., 2020, 2021\)](#). During the estimation stage of Algorithm 2, we simulate conditionally on a partially observed field using a checkerboard Gibbs sampler (see Section S5 of the Supplementary Material). As in Section 3.2, we consider estimation under missingness according to both MCAR and MICB models.

Table 2 and Figure 4 report our results for NBEs of the Potts Model’s parameter β . As for the Gaussian process model, the EM NBE is agnostic to the missingness pattern and

performs well under both missingness models considered in this experiment. By contrast, the Masking NBE is biased for most values of β when the missingness model is misspecified.

4 Application

Here, we consider a remote-sensing application with Arctic sea-ice data. These data are high-dimensional, and the missingness mechanism is difficult to model, but these challenges can be overcome using the EM NBE (Algorithm 2).

Arctic sea ice plays an important role in regulating our climate: it acts as a reflective surface that reduces the amount of solar energy absorbed by Earth. Melting sea ice exposes darker ocean water, thereby further accelerating the melting process due to an albedo-ice feedback effect. Changes in Arctic sea ice extent and thickness also affect atmospheric circulation and ocean currents, which can influence weather patterns worldwide (Cvijanovic et al., 2017). Further, Arctic sea ice provides vital habitats for species such as polar bears and seals, and its loss can disrupt fragile ecosystems, thereby affecting biodiversity, food webs, and fisheries (Meier et al., 2014). Understanding the temporal evolution of Arctic sea ice is therefore crucial for informing policies aimed at mitigating the impacts of climate change, managing resources sustainably, and protecting vulnerable ecosystems (United Nations, 2024).

In this application, we consider data of Arctic sea-ice concentrations (proportion of sea ice in a grid cell) produced by the National Oceanic and Atmospheric Administration (NOAA) as part of their National Snow and Ice Data Center’s (NSIDC) Climate Data Record (CRD; Meier et al., 2021). The data are derived from passive microwave remote sensing data provided by the Nimbus 7 satellite and the F8, F11, F13, and F17 satellites of the Defence Meteorological Satellite Program, projected onto $25\text{km} \times 25\text{km}$ grid cells within a region of the Northern Hemisphere spanning longitudes 180°E to 180°W (Meier et al., 2021). Following Zhang and Cressie (2020) (and numerous other studies of sea-ice extents; see, e.g., Parkinson, 2014), we apply a 15% cut-off to classify a grid cell as “Ice” (ice area $\geq 15\%$) or “Not ice” (ice area $< 15\%$). Arctic-sea-ice cover typically reaches its annual minimum in the month of September (Parkinson, 2014), and we therefore base our analysis on the ice cover on the first day of September in each year. In September, sea ice does not appear below latitude 60°N (Zhang and Cressie, 2020), and we therefore only consider those grid cells with latitude at or above 60°N . Our preprocessed data set comprises 45 spatial images (one image for each year between 1979 and 2023), with each image containing $199 \times 219 = 43581$ grid cells, and we analyze each year separately.

Figure 5 shows that the data are incomplete, and that the missingness patterns are relatively complicated. Here, missingness occurs for several reasons, including cloud cover and unpredictable issues with the remote-sensing instrument (Meier et al., 2021). The data are also subject to a more consistent form of missingness around the North Pole: this area, called the Arctic Pole Hole, changes in size over time as it is a function of both the remote-sensing instrument and the prevailing atmospheric conditions (Meier et al., 2021).

We model these Arctic sea-ice data using the Ising model (i.e., the Potts model characterized by (18) with $Q = 2$) with states “Ice” and “Not ice”. Recall that, at the critical value $\beta_c = \log(1 + \sqrt{Q}) \approx 0.881$, the Potts model undergoes a phase transition from disorder when $\beta < \beta_c$ to order when $\beta > \beta_c$. The images shown in Figure 5 indicate strong clustering,

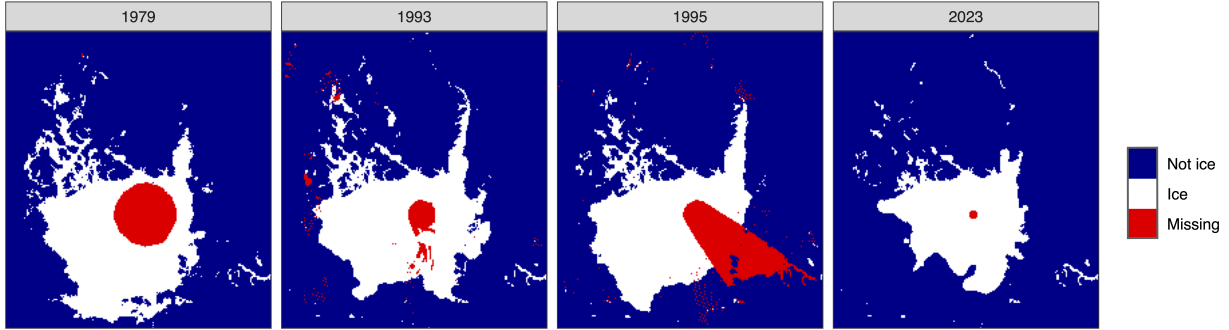


Figure 5: Arctic sea-ice data from the first day of September for the years 1979, 1993, 1995, and 2023. The data are subject to both random sources of missingness (e.g., cloud cover) and more consistent sources of missingness due to remote-sensing limitations (e.g., the Arctic Pole Hole).

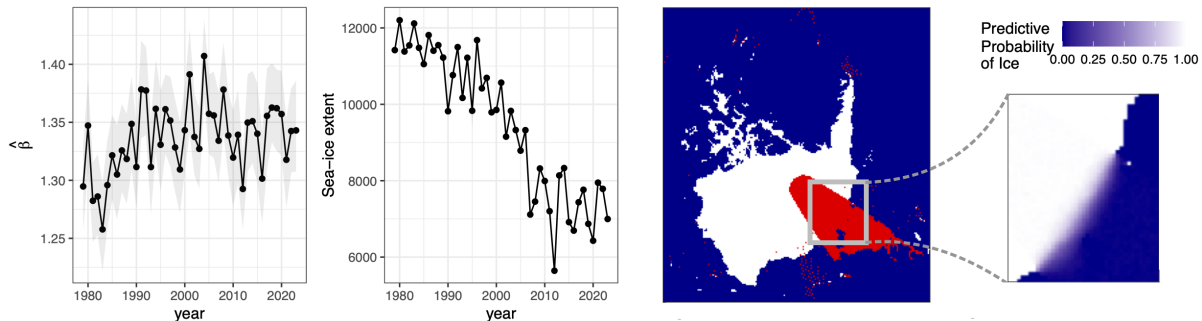


Figure 6: Analysis of Arctic sea-ice data. (Left) Neural EM estimates of the spatial dependence parameter β in (18) versus year. Shaded areas display 95% pointwise confidence intervals obtained using parametric bootstrap sampling. (Center-left) Predictions of sea-ice extent (the number of grid cells labeled as ice) versus year. Note that 95% prediction intervals are plotted, but these are not visible due to the low uncertainty in the predictions. (Center-right) Arctic sea-ice data from the first day of September 1995. (Right) Predictive probability that a grid cell is labeled as ice, for all grid cells within the gray box of the center-right panel (observed pixels are assigned a probability of 1 or 0 according to whether ice was observed or not).

and one could therefore consider a prior with support $\beta > \beta_c$. However, to remain general, we adopt a noninformative prior, $\beta \sim \text{Unif}(0, 1.5)$. Given the large data size, the computationally intractable model, and the complicated missingness mechanisms, our EM NBE (Algorithm 2) is well-suited for making inference in this application. We trained it using the same settings given in Section 3.3, with a total training time (including data simulation) of 24 minutes. We then applied the EM NBE to each of the 45 images. The total time for estimating the 45 Potts Model parameters $\{\beta_t : t = 1, \dots, 45\}$ was 3.6 seconds.

Figure 6, left panel, shows estimates $\{\hat{\beta}_t : t = 1, \dots, 45\}$, as well as 95% pointwise confidence intervals. To obtain these intervals, we used a separate parametric bootstrap for each year. Specifically, for each year, we simulated 400 data sets from the fitted model, removed data from the same grid cells that were missing in the observed data set, and then applied the EM NBE again to each of the 400 simulated (incomplete) data sets. All estimates are considerably larger than the critical value $\beta_c \approx 0.881$, confirming a strong tendency for

neighboring grid cells to share the same label.

Figure 6, center-left panel, shows predictions of sea-ice extent (the total number of pixels labeled as ice) as a function of year. To make these predictions, we imputed missing values by simulating 400 times from the fitted model (of the corresponding year) conditionally on the observed data, and we used the mean of these conditional simulations as the prediction. In line with the general scientific consensus, our analysis indicates that sea-ice extent is decreasing dramatically over time, nearly halving over the study period. The center-right and right panels of Figure 6 show the incomplete data from the first day of September 1995 and the resulting predictive probabilities of ice in a box containing a subset of the incomplete data. Due to the strong spatial dependence, the predictive probabilities in the interior of the ice sheet and in regions far from ice are close to 1 and 0, respectively; however, there is greater variability within the region corresponding to the sea-ice boundary. Post-training, inference (including bootstrap) for all 45 years of data took a total of 24 minutes clock time, compared to Zhang and Cressie’s (2020) fully Bayesian inference that took more than a day for fewer years.

5 Conclusion

Incomplete data are ubiquitous in applications of AI, arising from various sources such as cloud cover, equipment malfunctions, and data corruption. In this article, we focus on the problem of missing data in the context of neural Bayes estimation, which uses neural networks to map data to parameter point estimates. We first discuss and give new insights on the masking approach of Wang et al. (2024) (Algorithm 1), where inference is performed on an extended data set containing the observed data and auxiliary variables that encode the missingness pattern. This approach can be used to quickly generate Bayes estimates under general loss functions; it only requires marginal (i.e., unconditional) simulation from the data model; it is theoretically well motivated (see Theorem 1 in Section S1 of the Supplementary Material); and it performs well when the data are low-dimensional (see Section S6 of the Supplementary Material, where we analyze trivariate cryptocurrency data). However, it requires a model for the missingness mechanism, which can lead to bias and statistical inefficiency when the data are high-dimensional. We therefore propose an alternative approach that is based on the Monte Carlo EM algorithm, where the E- and M-steps are approximated using conditional simulation and an NBE that returns the MAP estimate from the conditionally-completed data. Our EM approach (Algorithm 2) is likelihood-free, in the sense that it does not require evaluation or knowledge of the likelihood function; it is fast, since it does not require numerical optimization at each iteration; and, in contrast to the masking approach, it is agnostic to the missingness pattern of the observed data. This research therefore represents a prototype problem that indicates how improvements could be made in AI by introducing statistical inferential tools.

Our EM approach to neural Bayes estimation with incomplete data is likelihood-free but reliant on conditional simulation, which can be a computational bottleneck for certain models. Future research will explore the use of neural conditional simulation (e.g., Wu et al., 2023) to extend the applicability of our EM approach to models for which conditional simulation is intractable or computationally prohibitive. Future research will also explore

computationally efficient conditional simulation from Markov random fields based on the construction given in Kaiser and Cressie (2000). It would also be useful to see how missing data can be handled within the censoring framework of Richards et al. (2025). While we focus on point estimation, our insights on the masking approach extend to methods that use it to approximate the full posterior distribution of the parameters (e.g., Radev et al., 2022) and more general inference frameworks (e.g., Gloeckler et al., 2024). In these contexts, the data-augmentation algorithm of Tanner and Wong (1987) offers advantages analogous to those of our EM approach in the point-estimation setting.

Acknowledgements

The authors thank Matthew Moores for discussion on, and code relating to, the Potts model.

Funding

MSD’s research was supported by an Australian Government Research Training Program Scholarship. MSD, AZM, and RH were supported by the KAUST Opportunity Fund Program ORFS-2023-OFP-5550.2. AZM’s research was supported by Australian Research Council (ARC) Discovery Early Career Research Award, DE180100203. AZM and NC were supported by ARC Discovery Project (DP), DP190100180. RH was also partially supported by KAUST Office of Sponsored Research (OSR) under Award No. OSR-CRG2020-4394. This material is based upon work supported by the Air Force Office of Scientific Research under award number FA2386-23-1-4100 (AZM and NC).

References

- Besag, J. (1972). Nearest-neighbour systems and the auto-logistic model for binary data. *Journal of the Royal Statistical Society B*, 34:75–83.
- Besag, J. (1974). Spatial interaction and the statistical analysis of lattice systems. *Journal of the Royal Statistical Society B*, 36:192–225.
- Booth, J. G. and Hobert, J. P. (1999). Maximizing generalized linear mixed model likelihoods with an automated Monte Carlo EM algorithm. *Journal of the Royal Statistical Society B*, 61:265–285.
- Boyles, R. A. (1983). On the convergence of the EM algorithm. *Journal of the Royal Statistical Society B*, 45:47–50.
- Breiman, L. (1996). Bagging predictors. *Machine Learning*, 24:123–140.
- Caffo, B. S., Crainiceanu, C. M., and Richardson, B. A. (2005). Predictive convergence and consistency of Monte Carlo EM in high-dimensional latent variable models. *Journal of Computational and Graphical Statistics*, 14:804–834.
- Chan, K.-S. and Ledolter, J. (1995). Monte Carlo EM estimation for time series models involving counts. *Journal of the American Statistical Association*, 90:242–252.
- Chen, Y., Zhang, D., Gutmann, M. U., Courville, A., and Zhu, Z. (2021). Neural approximate sufficient statistics for implicit models. In *Proceedings of the 9th International Conference on Learning Representations (ICLR 2021)*. Virtual: OpenReview. <https://openreview.net/forum?id=SRDuJssQud>.

- Cox, D. R. and Hinkley, D. V. (1974). *Theoretical Statistics*. Chapman and Hall, New York, NY.
- Cranmer, K., Brehmer, J., and Louppe, G. (2020). The frontier of simulation-based inference. *Proceedings of the National Academy of Sciences*, 117:30055–30062.
- Cressie, N. (1993). *Statistics for Spatial Data*, revised edition. Wiley, Hoboken, NJ.
- Cvijanovic, I., Santer, B. D., Bonfils, C., Lucas, D. D., JCH, C., and Zimmerman, S. (2017). Future loss of Arctic sea-ice cover could drive a substantial decrease in California’s rainfall. *Nature Communications*, 8:1947.
- Dell’Oro, L. and Gaetan, C. (2024). Flexible space-time models for extreme data. <https://doi.org/10.48550/arXiv.2411.19184>.
- Dempster, A. P., Laird, N. M., and Rubin, D. B. (1977). Maximum likelihood from incomplete data via the EM algorithm. *Journal of the Royal Statistical Society B*, 39:1–38.
- Diggle, P. J. and Gratton, R. J. (1984). Monte Carlo methods of inference for implicit statistical models. *Journal of the Royal Statistical Society B*, 46:193–227.
- Flagel, L., Brandvain, Y., and Schrider, D. R. (2018). The unreasonable effectiveness of convolutional neural networks in population genetic inference. *Molecular Biology and Evolution*, 36:220–238.
- Fort, G. and Moulines, E. (2003). Convergence of the Monte Carlo expectation maximization for curved exponential families. *Annals of Statistics*, 31:1220–1259.
- Gelfand, A. E. and Smith, A. F. M. (1990). Sampling-based approaches to calculating marginal densities. *Journal of the American Statistical Association*, 85:398–409.
- Gerber, F. and Nychka, D. W. (2021). Fast covariance parameter estimation of spatial Gaussian process models using neural networks. *Stat*, 10:e382.
- Glöckler, M., Deistler, M., and Macke, J. H. (2022). Variational methods for simulation-based inference. In *Proceedings of the 10th International Conference on Learning Representations (ICLR 2022)*. Virtual: OpenReview. <https://openreview.net/forum?id=kZOUYdhqkNY>.
- Gloekler, M., Deistler, M., Weilbach, C., Wood, F., and Macke, J. H. (2024). All-in-one simulation-based inference. In Salakhutdinov, R., Kolter, Z., Heller, K., Weller, A., Oliver, N., Scarlett, J., and Berkenkamp, F., editors, *Proceedings of the 41st Conference on Machine Learning*, volume 235, pages 15735–15766.
- Gonçalves, P. J., Lueckmann, J.-M., Deistler, M., Nonnenmacher, M., Öcal, K., Bassetto, G., Chintaluri, C., Podlaski, W. F., Haddad, S. A., Vogels, T. P., Greenberg, D. S., and Macke, J. H. (2020). Training deep neural density estimators to identify mechanistic models of neural dynamics. *eLife*, 9:e56261.
- Greenberg, D., Nonnenmacher, M., and Macke, J. (2019). Automatic posterior transformation for likelihood-free inference. In Chaudhuri, K. and Salakhutdinov, R., editors, *Proceedings of the 36th International Conference on Machine Learning*, volume 97 of *Proceedings of Machine Learning Research*, pages 2404–2414.
- Guinness, J. (2018). Permutation and grouping methods for sharpening Gaussian process approximations. *Technometrics*, 60:415–429.
- Hansen, L. K. and Salamon, P. (1990). Neural network ensembles. *IEEE Transactions on Pattern Analysis and Machine Intelligence*, 12:993–1001.
- Hardie, R., Eismann, M., and Wilson, G. (2004). MAP estimation for hyperspectral image resolution enhancement using an auxiliary sensor. *IEEE Transactions on Image Processing*, 13:1174–1184.
- Hermans, J., Begy, V., and Louppe, G. (2020). Likelihood-free MCMC with amortized approximate ratio estimators. In Daumé III, H. and Singh, A., editors, *Proceedings of the 37th International*

- Conference on Machine Learning*, volume 119 of *Proceedings of Machine Learning Research*, pages 4239–4248.
- Hernandez, A. (2017). Model calibration with neural networks. *Risk*. <http://dx.doi.org/10.2139/ssrn.2812140>.
- Hornik, K., Stinchcombe, M., and White, H. (1989). Multilayer feedforward networks are universal approximators. *Neural Networks*, 2:359–366.
- Horvath, B., Muguruza, A., and Tomas, M. (2021). Deep learning volatility: a deep neural network perspective on pricing and calibration in (rough) volatility models. *Quantitative Finance*, 21:11–27.
- Ising, E. (1925). *Beitrag zur Theorie des Ferromagnetismus*. PhD thesis, Universität Hamburg, Hamburg, Germany.
- Jamshidian, F. and Jennrich, R. I. (1997). Acceleration of the EM algorithm by using quasi-Newton methods. *Journal of the Royal Statistical Society B*, 59:569–587.
- Kaiser, M. S. and Cressie, N. (2000). The construction of multivariate distributions from Markov random fields. *Journal of Multivariate Analysis*, 73:199–220.
- Lehmann, E. L. and Casella, G. (1998). *Theory of Point Estimation*, 2nd edition. Springer, New York, NY.
- Lenzi, A., Bessac, J., Rudi, J., and Stein, M. L. (2023). Neural networks for parameter estimation in intractable models. *Computational Statistics & Data Analysis*, 185:107762.
- Levine, R. A. and Casella, G. (2001). Implementations of the Monte Carlo EM algorithm. *Journal of Computational and Graphical Statistics*, 10:422–439.
- Lewandowski, D., Kurowicka, D., and Joe, H. (2009). Generating random correlation matrices based on vines and extended onion method. *Journal of Multivariate Analysis*, 100:1989–2001.
- Liu, J. S. and Rubin, D. B. (1994). The ECME algorithm: A simple extension of EM and ECM with faster monotone convergence. *Biometrika*, 81:633–648.
- Louis, T. A. (1982). Finding the observed information matrix when using the EM algorithm. *Journal of the Royal Statistical Society B*, 44:226–233.
- Maceda, E., Hector, E. C., Lenzi, A., and Reich, B. J. (2024). A variational neural Bayes framework for inference on intractable posterior distributions. <https://doi.org/10.48550/arXiv.2404.10899>.
- Marin, J.-M. and Robert, C. P. (2007). *Bayesian Core: A Practical Approach to Computational Bayesian Statistics*. Springer, New York, NY.
- McCulloch, C. E. (1997). Maximum likelihood algorithms for generalized linear mixed models. *Journal of the American Statistical Association*, 92:162–170.
- McLachlan, G. J. and Krishnan, T. (2007). *The EM Algorithm and Extensions*, 2nd edition. Wiley, Hoboken, NJ.
- Meier, W. N., Fetterer, F., Windnagel, A. K., and Stewart, J. S. (2021). *NOAA/NSIDC Climate Data Record of Passive Microwave Sea Ice Concentration, Version 4. Northern Hemisphere*. NSIDC: National Snow and Ice Data Center, Boulder, Colorado USA. <https://doi.org/10.7265/efmz-2t65>.
- Meier, W. N., Hovelsrud, G. K., Oort, B. E., Key, J. R., Kovacs, K. M., Michel, C., Haas, C., Granskog, M. A., Gerland, S., Perovich, D. K., et al. (2014). Arctic sea ice in transformation: A review of recent observed changes and impacts on biology and human activity. *Reviews of Geophysics*, 52:185–217.
- Meng, X.-L. and Rubin, D. B. (1993). Maximum likelihood estimation via the ECM algorithm: A general framework. *Biometrika*, 80:267–278.

- Montesinos-López, A., Gutierrez-Pulido, H., Montesinos-López, O. A., and Crossa, J. (2020). Maximum a posteriori threshold genomic prediction model for ordinal traits. *G3*, 10:4083–4102.
- Moore, M. T., Feng, D., and Mengersen, K. (2021). *bayesImageS: Bayesian Methods for Image Segmentation using a Potts Model*. R package version 0.6.1, <https://CRAN.R-project.org/package=bayesImageS>.
- Moore, M. T., Pettitt, A. N., and Mengersen, K. (2020). Bayesian computation with intractable likelihoods. In Mengersen, K. L., Pudlo, P., and Robert, C. P., editors, *Case Studies in Applied Bayesian Data Science*, pages 137–151. Springer, New York, NY.
- Neal, R. M. and Hinton, G. E. (1998). A view of the EM algorithm that justifies incremental, sparse, and other variants. In Jordan, M. I., editor, *Learning in Graphical Models*, pages 355–368. Springer, New York, NY.
- Neath, R. C. (2013). On convergence properties of the Monte Carlo EM algorithm. In *Advances in Modern Statistical Theory and Applications: A Festschrift in Honor of Morris L. Eaton*, volume 10, pages 43–62. Institute of Mathematical Statistics.
- Onsager, L. (1944). Crystal statistics. I. A two-dimensional model with an order-disorder transition. *Physical Review*, 65:117–149.
- OpenAI (2023). ChatGPT. <https://openai.com/chatgpt>.
- Pacchiardi, L. and Dutta, R. (2022). Likelihood-free inference with generative neural networks via scoring rule minimization. <https://doi.org/10.48550/arXiv.2205.15784>.
- Pan, T.-F., Li, J.-J., Thompson, B., and Collins, A. (2024). Latent variable sequence identification for cognitive models with neural Bayes estimation. <https://doi.org/10.48550/arXiv.2406.14742>.
- Papamakarios, G., Sterratt, D., and Murray, I. (2019). Sequential neural likelihood: Fast likelihood-free inference with autoregressive flows. In Chaudhuri, K. and Sugiyama, M., editors, *Proceedings of the Twenty-Second International Conference on Artificial Intelligence and Statistics*, volume 89 of *Proceedings of Machine Learning Research*, pages 837–848.
- Parkinson, C. L. (2014). Global sea ice coverage from satellite data: Annual cycle and 35-yr trends. *Journal of Climate*, 27:9377–9382.
- Potts, R. B. (1952). Some generalized order-disorder transformations. *Mathematical Proceedings of the Cambridge Philosophical Society*, 48:106–109.
- Radev, S. T., Mertens, U. K., Voss, A., Ardizzone, L., and Köthe, U. (2022). BayesFlow: Learning complex stochastic models with invertible neural networks. *IEEE Transactions on Neural Networks and Learning Systems*, 33:1452–1466.
- Radev, S. T., Schmitt, M., Pratz, V., Picchini, U., Köthe, U., and Bürkner, P.-C. (2023). JANA: Jointly amortized neural approximation of complex Bayesian models. In Evans, R. J. and Shpitser, I., editors, *Proceedings of the Thirty-Ninth Conference on Uncertainty in Artificial Intelligence*, volume 216 of *Proceedings of Machine Learning Research*, pages 1695–1706.
- Ramesh, P., Lueckmann, J.-M., Boelts, J., Tejero-Cantero, Á., Greenberg, D. S., Gonçalves, P. J., and Macke, J. H. (2022). GATSBI: Generative adversarial training for simulation-based inference. In *Proceedings of the 10th International Conference on Learning Representations (ICLR 2022)*. Virtual: OpenReview. <https://openreview.net/forum?id=kR1hC6j48Tp>.
- Reich, B. J. and Shaby, B. A. (2018). A spatial Markov model for climate extremes. *Journal of Computational and Graphical Statistics*, 28:117–126.
- Richards, J., Sainsbury-Dale, M., Huser, R., and Zammit-Mangion, A. (2025). Neural Bayes estimators for censored inference with peaks-over-threshold models. *Journal of Machine Learning Research*, to appear. <https://doi.org/10.48550/arXiv.2306.15642>.
- Robert, C. P. (2007). *The Bayesian Choice*, 2nd edition. Springer, New York, NY.

- Rudi, J., Julie, B., and Lenzi, A. (2021). Parameter estimation with dense and convolutional neural networks applied to the FitzHugh-Nagumo ODE. In Bruna, J., Hesthaven, J., and Zdeborova, L., editors, *Proceedings of the 2nd Annual Conference on Mathematical and Scientific Machine Learning*, volume 145 of *Proceedings of Machine Learning Research*, pages 1–28.
- Rue, H. and Held, L. (2005). *Gaussian Markov Random Fields: Theory and Applications*. CRC Press, Boca Raton, FL.
- Ruth, W. (2024). A review of Monte Carlo-based versions of the EM algorithm. <https://doi.org/10.48550/arXiv.2401.00945>.
- Sainsbury-Dale, M. (2024). *NeuralEstimators: Likelihood-Free Parameter Estimation using Neural Networks*. R package version 0.1.2, <https://CRAN.R-project.org/package=NeuralEstimators>.
- Sainsbury-Dale, M., Zammit-Mangion, A., and Huser, R. (2024). Likelihood-free parameter estimation with neural Bayes estimators. *The American Statistician*, 78:1–14.
- Sainsbury-Dale, M., Zammit-Mangion, A., Richards, J., and Huser, R. (2025). Neural Bayes estimators for irregular spatial data using graph neural networks. *Journal of Computational and Graphical Statistics*, to appear. <https://doi.org/10.1080/10618600.2024.2433671>.
- Swendsen, R. H. and Wang, J.-S. (1987). Nonuniversal critical dynamics in Monte Carlo simulations. *Physical Review Letters*, 58:86–88.
- Tanner, M. A. and Wong, W. H. (1987). The calculation of posterior distributions by data augmentation. *Journal of the American Statistical Association*, 82:528–540.
- Tanner, M. A. and Wong, W. H. (2010). From EM to data augmentation: The emergence of MCMC Bayesian computation in the 1980s. *Statistical Science*, 25:506–516.
- Thomas, O., Dutta, R., Corander, J., Kaski, S., and Gutmann, M. U. (2022). Likelihood-free inference by ratio estimation. *Bayesian Analysis*, 17:1–31.
- Tsyrlunikov, M. and Sotskiy, A. (2024). Regularization of the ensemble Kalman filter using a non-parametric, non-stationary spatial model. <https://doi.org/10.48550/arXiv.2306.14318>.
- United Nations (2024). Sustainable Development Goals. <https://sdgs.un.org/goals>.
- van der Vaart, A. W. (1998). *Asymptotic Statistics*. Cambridge University Press, Cambridge, UK.
- van Dyk, D. A. and Meng, X.-L. (2001). The art of data augmentation. *Journal of Computational and Graphical Statistics*, 10:1–50.
- Varadhan, R. and Roland, C. (2008). Simple and globally convergent methods for accelerating the convergence of any EM algorithm. *Scandinavian Journal of Statistics*, 35:335–353.
- Vecchia, A. V. (1988). Estimation and model identification for continuous spatial processes. *Journal of the Royal Statistical Society B*, 50:297–312.
- Villazón, A., Alegría, A., and Emery, X. (2024). Neural networks for parameter estimation in geometrically anisotropic geostatistical models. <https://doi.org/10.48550/arXiv.2408.10915>.
- Vu, Q., Moores, M. T., and Zammit-Mangion, A. (2021). Warped gradient-enhanced Gaussian process surrogate models for exponential family likelihoods with intractable normalizing constants. <https://doi.org/10.48550/arXiv.2105.04374>.
- Wagstaff, E., Fuchs, F. B., Engelcke, M., Osborne, M., and Posner, I. (2022). Universal approximation of functions on sets. *Journal of Machine Learning Research*, 23:1–56.
- Walchessen, J., Lenzi, A., and Kuusela, M. (2024). Neural likelihood surfaces for spatial processes with computationally intensive or intractable likelihoods. *Spatial Statistics*, 62:100848.
- Wang, K. and Genton, M. G. (2024). A generalized unified skew-normal process with neural Bayes inference. <https://doi.org/10.48550/arXiv.2411.17400>.
- Wang, Z., Hasenauer, J., and Schälte, Y. (2024). Missing data in amortized simulation-based neural posterior estimation. *PLOS Computational Biology*, 20:e1012184.

- Wei, G. C. G. and Tanner, M. A. (1990). A Monte Carlo implementation of the EM algorithm and the poor man’s data augmentation algorithms. *Journal of the American Statistical Association*, 85:699–704.
- Wu, C. F. J. (1983). On the convergence properties of the EM algorithm. *Annals of Statistics*, 11:95–103.
- Wu, L., Trippe, B. L., Naesseth, C. A., Blei, D. M., and Cunningham, J. P. (2023). Practical and asymptotically exact conditional sampling in diffusion models. In Oh, A., Naumann, T., Globerson, A., Saenko, K., Hardt, M., and Levine, S., editors, *Proceedings of the 36th Conference on Neural Information Processing Systems*, pages 31372–31403, Red Hook, NY.
- Zaheer, M., Kottur, S., Ravanbakhsh, S., Poczos, B., Salakhutdinov, R. R., and Smola, A. J. (2017). Deep sets. In Guyon, I., Luxburg, U. V., Bengio, S., Wallach, H., Fergus, R., Vishwanathan, S., and Garnett, R., editors, *Proceedings of the 30th Conference on Neural Information Processing Systems*, pages 3392–3402, Red Hook, NY.
- Zammit-Mangion, A., Sainsbury-Dale, M., and Huser, R. (2025). Neural methods for amortized inference. *Annual Review of Statistics and Its Application*, to appear. <https://doi.org/10.48550/arXiv.2404.12484>.
- Zhang, B. and Cressie, N. (2020). Bayesian inference of spatio-temporal changes of Arctic sea ice. *Bayesian Analysis*, 15:605–631.
- Zhou, D. (2020). Universality of deep convolutional neural networks. *Applied and Computational Harmonic Analysis*, 48:787–794.

Supplementary Material for “Neural Parameter Estimation with Incomplete Data”

In Section S1, we provide a theoretical rationale for the masking approach of Wang et al. (2024). In Section S2, we consider several continuous approximations of the 0–1 loss function that may be used when training an NBE to approximate the MAP estimator. In Section S3, we illustrate the benefits of using an ensemble of deep neural networks in the context of neural Bayes estimation. In Section S4, we show that a single CNN-based NBE can be used with gridded data where grids are of varying size and shape. In Section S5, we describe the checkerboard Gibbs sampler used to sample from the Potts model in Section 3.3 and Section 4 of the main text. In Section S6, we employ the generalized hyperbolic distribution, fitted using our proposed neural EM algorithm, to analyze cryptocurrency data. Finally, in Section S7, we provide additional figures.

S1 Rationale for the masking approach

Here, we use a sufficiency argument to show that the masking approach of Wang et al. (2024) does not, in theory, lead to any loss of information on θ .

Theorem 1. *Let the complete data $\mathbf{Z} \in \mathbb{R}^n$ be distributed according to a family of probability distributions indexed by θ . Assume that \mathbf{Z} is partitioned into components \mathbf{Z}_1 and \mathbf{Z}_2 of observed and missing elements, respectively, and define the ordered set $\mathcal{I}_1 \equiv \{i : Z_i \text{ is observed}\}$ such that $\mathbf{Z}_1 = (Z_i : i \in \mathcal{I}_1)'$. Let \mathbf{U} and \mathbf{W} be defined as in Equations (4) and (5) of the main text. Then,*

$$\mathbf{T}(\mathbf{Z}_1, \mathcal{I}_1) \equiv (\mathbf{U}, \mathbf{W}),$$

is a sufficient statistic for θ .

Proof. Given that \mathbf{Z}_1 and \mathcal{I}_1 represent all of the available information from which to make inference on θ , that is, together they are sufficient for θ , we need only show that $\mathbf{T}(\cdot, \cdot)$ defines a one-to-one mapping from the space of $(\mathbf{Z}_1, \mathcal{I}_1)$ to that of (\mathbf{U}, \mathbf{W}) , since any one-to-one transformation of a sufficient statistic is itself sufficient (Casella and Berger, 2001, pg. 280). First, note that the construction of \mathbf{U} using Equation (4) of the main text can be equivalently written as $\mathbf{U} = \mathbf{Z} \odot \mathbf{W} + c(\mathbf{1} - \mathbf{W})$, where \odot denotes elementwise multiplication, and $\mathbf{1}$ denotes the vector of all 1s of appropriate dimension. Now, for any \mathbf{Z}_1^a and \mathcal{I}_1^a , and any \mathbf{Z}_1^b and \mathcal{I}_1^b ,

$$\begin{aligned} \mathbf{T}(\mathbf{Z}_1^a, \mathcal{I}_1^a) = \mathbf{T}(\mathbf{Z}_1^b, \mathcal{I}_1^b) &\implies (\mathbf{U}^a, \mathbf{W}^a) = (\mathbf{U}^b, \mathbf{W}^b) \\ &\implies \mathbf{U}^a = \mathbf{U}^b \text{ and } \mathbf{W}^a = \mathbf{W}^b \\ &\implies \mathbf{Z}^a \odot \mathbf{W}^a + c(\mathbf{1} - \mathbf{W}^a) = \mathbf{Z}^b \odot \mathbf{W}^a + c(\mathbf{1} - \mathbf{W}^a) \text{ and } \mathcal{I}_1^a = \mathcal{I}_1^b \\ &\implies \mathbf{Z}^a \odot \mathbf{W}^a = \mathbf{Z}^b \odot \mathbf{W}^a \text{ and } \mathcal{I}_1^a = \mathcal{I}_1^b \\ &\implies \mathbf{Z}_1^a = \mathbf{Z}_1^b \text{ and } \mathcal{I}_1^a = \mathcal{I}_1^b. \end{aligned}$$

Therefore, $\mathbf{T}(\cdot, \cdot)$ defines a one-to-one mapping from the space of $(\mathbf{Z}_1, \mathcal{I}_1)$ to that of (\mathbf{U}, \mathbf{W}) and, hence, $\mathbf{T}(\mathbf{Z}_1, \mathcal{I}_1)$ is sufficient for $\boldsymbol{\theta}$. \square

However, using \mathbf{U} and \mathbf{W} in place of \mathbf{Z}_1 and \mathcal{I}_1 in a neural Bayes estimation setting requires assigning a distribution to \mathcal{I}_1 , and misspecification of this distribution can lead to a highly biased estimator, as demonstrated in Section 3 of the main text. For further discussion, see Section 2.2 of the main text.

S2 Continuous approximations of the 0–1 loss function

In Section 2.3.3 of the main text, we describe how an NBE may be constructed to approximate the MAP estimator. The approach hinges on the use of a continuous approximation of the 0–1 loss function. In this section, we consider several candidate loss functions.

The loss function

$$L(\boldsymbol{\theta}, \hat{\boldsymbol{\theta}}; \beta) = (\|\hat{\boldsymbol{\theta}} - \boldsymbol{\theta}\|)^\beta, \quad \beta > 0, \quad (\text{S1})$$

where $\|\cdot\|$ denotes any norm in \mathbb{R}^p and p denotes the dimension of $\boldsymbol{\theta}$, generalizes the loss function given in Cressie (2022, Eqn. 6) to the multiparameter setting, and it yields the 0–1 loss in the limit as $\beta \rightarrow 0$. A possible surrogate for the 0–1 loss function is therefore given by (S1) with β close to zero. However, with $\beta < 1$, the gradient of (S1) diverges as $\|\hat{\boldsymbol{\theta}} - \boldsymbol{\theta}\| \rightarrow 0$, which can cause numerical instability during training. There are several ways to alleviate this issue. For instance, one may add a small positive constant δ to $\|\hat{\boldsymbol{\theta}} - \boldsymbol{\theta}\|$ in (S1), yielding the loss function,

$$L_{\text{POW}}(\boldsymbol{\theta}, \hat{\boldsymbol{\theta}}; \beta, \delta) = (\|\hat{\boldsymbol{\theta}} - \boldsymbol{\theta}\| + \delta)^\beta - \delta^\beta, \quad \beta > 0, \delta > 0, \quad (\text{S2})$$

Figure S1, panel A, shows (S2) and its gradient for $\beta \in \{1, 0.5, 0.1, 0.05\}$ and $\delta \in \{0, 0.1\}$.

Other continuous approximations are available, and in the main text, we adopt the loss function,

$$L_{\text{TANH}}(\boldsymbol{\theta}, \hat{\boldsymbol{\theta}}; \kappa) = \tanh(\|\hat{\boldsymbol{\theta}} - \boldsymbol{\theta}\|/\kappa), \quad \kappa > 0, \quad (\text{S3})$$

which, unlike (S2), only involves one tuning parameter. For this reason, we prefer the TANH approximation. Figure S1, panel B, shows (S3) and its gradient for $\kappa \in \{1, 0.5, 0.1, 0.05\}$. Figure S2 shows (S3) for $\boldsymbol{\theta} = (\theta_1, \theta_2)'$. For fixed κ , the gradient of (S3) is bounded as $\|\hat{\boldsymbol{\theta}} - \boldsymbol{\theta}\| \rightarrow 0$, and it yields the 0–1 loss function in the limit as $\kappa \rightarrow 0$, which we now prove.

Proof. From the definition of the hyperbolic tangent function, it follows that

$$\begin{aligned} L_{\text{TANH}}(\boldsymbol{\theta}, \hat{\boldsymbol{\theta}}; \kappa) &= \tanh(\|\hat{\boldsymbol{\theta}} - \boldsymbol{\theta}\|/\kappa) \\ &= \frac{\exp(\|\hat{\boldsymbol{\theta}} - \boldsymbol{\theta}\|/\kappa) - \exp(-\|\hat{\boldsymbol{\theta}} - \boldsymbol{\theta}\|/\kappa)}{\exp(\|\hat{\boldsymbol{\theta}} - \boldsymbol{\theta}\|/\kappa) + \exp(-\|\hat{\boldsymbol{\theta}} - \boldsymbol{\theta}\|/\kappa)}, \\ &= \frac{1 - \exp(-2\|\hat{\boldsymbol{\theta}} - \boldsymbol{\theta}\|/\kappa)}{1 + \exp(-2\|\hat{\boldsymbol{\theta}} - \boldsymbol{\theta}\|/\kappa)}. \end{aligned}$$

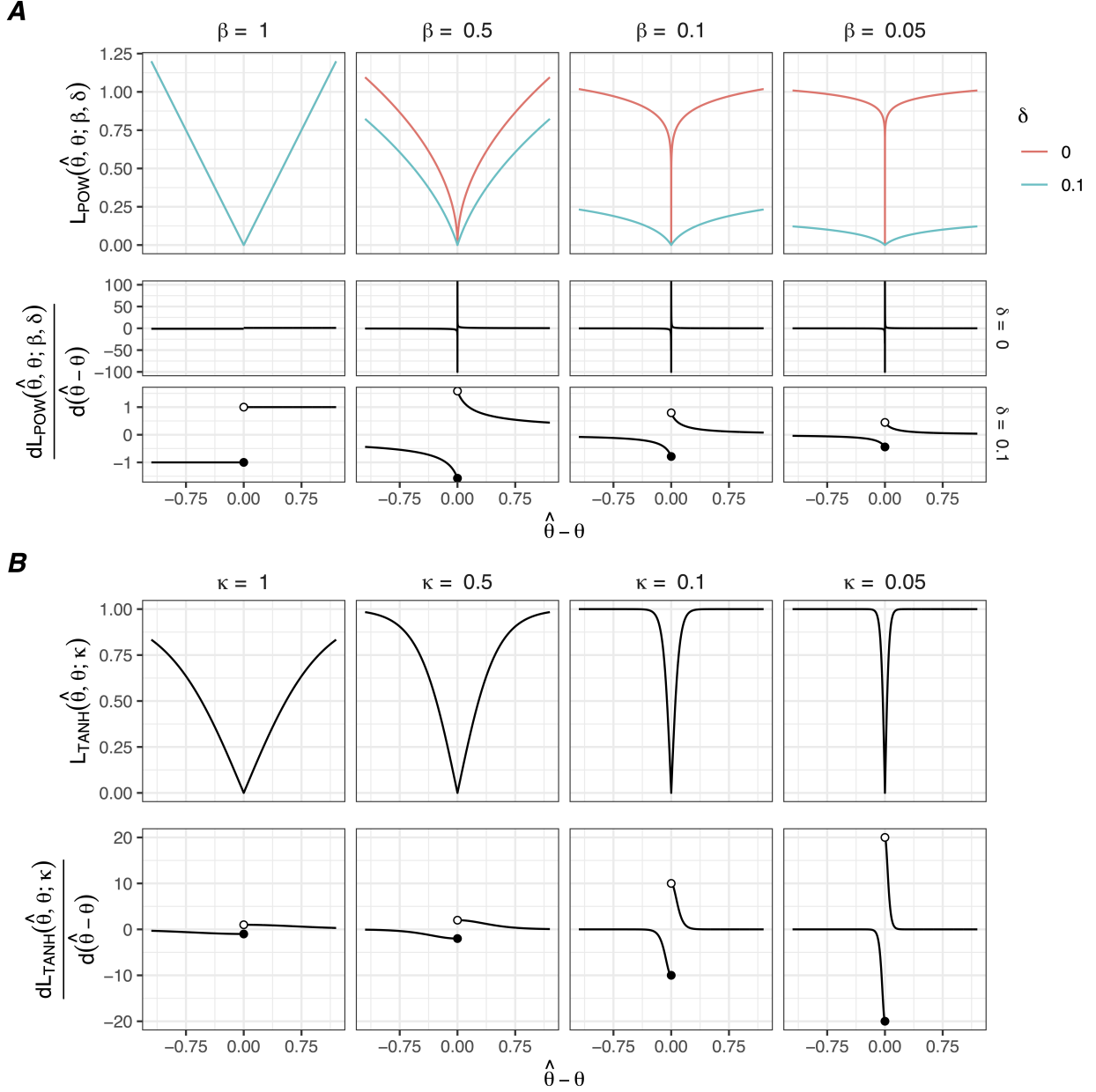


Figure S1: (A) The loss function (S2) and its gradient for $\beta \in \{1, 0.5, 0.1, 0.05\}$ and $\delta \in \{0, 0.1\}$. For $\delta = 0$ and $\beta < 1$, the gradient diverges at the origin; for $\delta = 0.1$, the gradient is finite and decreases as β decreases. (B) The loss function (S3) and its gradient for $\kappa \in \{1, 0.5, 0.1, 0.05\}$.

First, suppose that $\hat{\boldsymbol{\theta}} = \boldsymbol{\theta}$, so that $\|\hat{\boldsymbol{\theta}} - \boldsymbol{\theta}\| = 0$. In this case, we have that

$$L_{\text{TANH}}(\boldsymbol{\theta}, \hat{\boldsymbol{\theta}}; \kappa)|_{\hat{\boldsymbol{\theta}}=\boldsymbol{\theta}} = \frac{1 - \exp(0)}{1 + \exp(0)} = 0.$$

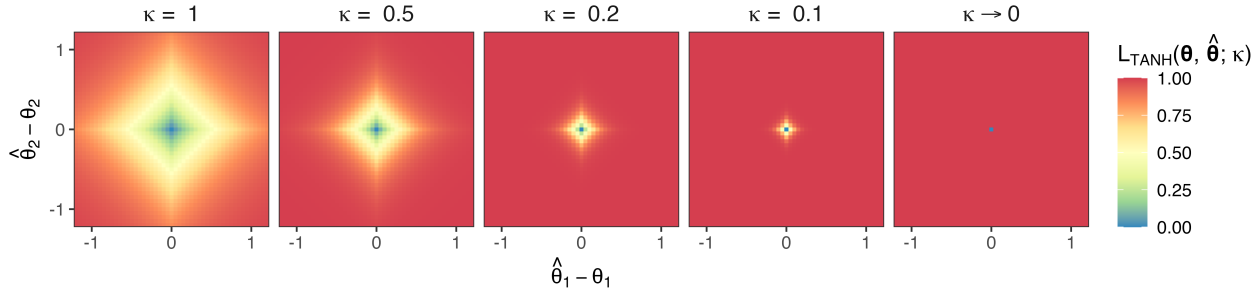


Figure S2: The loss function (S3) for $p = 2$ parameters and several choices of κ . The 0–1 loss is obtained in the limit as $\kappa \rightarrow 0$.

Second, suppose that $\hat{\boldsymbol{\theta}} \neq \boldsymbol{\theta}$, so that $\|\hat{\boldsymbol{\theta}} - \boldsymbol{\theta}\| > 0$. In this case, we have that

$$\lim_{\kappa \rightarrow 0} L_{\text{TANH}}(\boldsymbol{\theta}, \hat{\boldsymbol{\theta}}; \kappa) = \lim_{\kappa \rightarrow 0} \frac{1 - \exp(-2\|\hat{\boldsymbol{\theta}} - \boldsymbol{\theta}\|/\kappa)}{1 + \exp(-2\|\hat{\boldsymbol{\theta}} - \boldsymbol{\theta}\|/\kappa)} = 1,$$

since $\lim_{x \rightarrow \infty} e^{-ax} = 0$ for all $a > 0$. Therefore, we obtain

$$\lim_{\kappa \rightarrow 0} L_{\text{TANH}}(\boldsymbol{\theta}, \hat{\boldsymbol{\theta}}; \kappa) = \begin{cases} 0 & \text{if } \hat{\boldsymbol{\theta}} = \boldsymbol{\theta}, \\ 1 & \text{otherwise,} \end{cases}$$

which is the 0–1 loss function. □

Another possible surrogate loss function is given by

$$L_{\text{CORR}}(\boldsymbol{\theta}, \hat{\boldsymbol{\theta}}; \rho, \alpha) = 1 - \{1 + (\|\hat{\boldsymbol{\theta}} - \boldsymbol{\theta}\|/\rho)^\alpha\}^{-1}, \quad \rho > 0, \alpha \geq 1, \quad (\text{S4})$$

which yields the 0–1 loss in the limit as $\rho \rightarrow 0$, where the right-hand side of (S4) is a variogram constructed from the Cauchy correlation function (Gneiting and Schlather, 2004). Similar to (S2) and to (S3), for fixed ρ , the gradient of (S4) is bounded. In general, similarly constructed variogram models provide a broad family of functions that may serve as continuous approximations of the 0–1 loss function, with various degrees of differentiability at the origin that may be controlled by the practitioner. These classes are mentioned here for completeness; in this paper we use the loss function (S3), which we find to work well in practice.

S3 Ensembles of NBEs

An ensemble of neural networks (Hansen and Salamon, 1990; Breiman, 1996) consists of neural networks trained to solve the same task but with variations introduced during the training process. These variations could include different initial values for the neural-network parameters, different architectures, or different learning rates. The inference for an ensemble can be obtained by averaging the outputs of its individual networks, and it is often more accurate than that of any individual network.

In our case, we obtain an ensemble of J NBEs $\{\hat{\boldsymbol{\theta}}_{\gamma_j^*}(\cdot) : j = 1, \dots, J\}$ by using J different initial values for the neural-network parameters. We may posit the following working model to characterize the error of each NBE:

$$\hat{\boldsymbol{\theta}}_{\gamma_j^*}(\mathbf{Z}) = \hat{\boldsymbol{\theta}}_{\text{Bayes}}(\mathbf{Z}) + \epsilon_j(\mathbf{Z}), \quad \mathbf{Z} \in \mathcal{Z}, \quad j = 1, \dots, J, \quad (\text{S5})$$

where $\hat{\boldsymbol{\theta}}_{\text{Bayes}}(\mathbf{Z})$ is the Bayes estimate of $\boldsymbol{\theta}$ for the loss function being used, and $\epsilon_j(\mathbf{Z})$ is a mean-zero error term with variance σ_ϵ^2 . Then, the ensemble estimate is obtained as:

$$\hat{\boldsymbol{\theta}}_{\text{ensemble}}(\mathbf{Z}) \equiv \frac{1}{J} \sum_{j=1}^J \hat{\boldsymbol{\theta}}_{\gamma_j^*}(\mathbf{Z}), \quad \mathbf{Z} \in \mathcal{Z}. \quad (\text{S6})$$

Under our working model, for fixed $\mathbf{Z} \in \mathcal{Z}$,

$$\mathbb{E}\{\hat{\boldsymbol{\theta}}_{\text{ensemble}}(\mathbf{Z})\} = \hat{\boldsymbol{\theta}}_{\text{Bayes}}(\mathbf{Z}), \quad \text{var}\{\hat{\boldsymbol{\theta}}_{\text{ensemble}}(\mathbf{Z})\} = \sigma_\epsilon^2/J,$$

where the expectation and variance are taken over the ensemble estimates for a fixed \mathbf{Z} . In practice, the errors may not be mean-zero, nor independent; however, provided that they are not perfectly correlated, the ensemble estimate (S6) will still have reduced variance compared with estimates from individual ensemble members.

For illustration, we consider a spatial Gaussian process model, where $\mathbf{Z} \equiv (Z_1, \dots, Z_n)'$ are data collected at locations $\{\mathbf{s}_1, \dots, \mathbf{s}_n\}$ in a spatial domain \mathcal{D} . Assume the data are mean-zero Gaussian random variables with exponential spatial covariance function,

$$\text{cov}(Z_i, Z_j) = \exp(-\|\mathbf{s}_i - \mathbf{s}_j\|/\theta), \quad i, j = 1, \dots, n,$$

with $\text{var}(Z_i) = 1$ and unknown range parameter $\theta > 0$. Here, we take \mathcal{D} to be the unit square, we simulate data on a grid with $n = 16^2 = 256$ observation locations, and we adopt the prior $\theta \sim \text{Unif}(0, 0.5)$. Note that the data are completely observed in this experiment, where our aim is to show the utility of ensembles of NBEs.

Since our data are gridded, we construct our NBEs using convolutional neural networks (CNNs; see, e.g., Dumoulin and Visin, 2016; Goodfellow et al., 2016, Ch. 9). To demonstrate that the ensemble approach improves estimation across different neural-network architectures, we consider three architectures. The first architecture was used by Zammit-Mangion et al. (2025); it contains two convolutional layers and 150913 trainable parameters. The second architecture was proposed by Gerber and Nychka (2021) and subsequently used by Sainsbury-Dale et al. (2024) and Richards et al. (2025); it contains three convolutional layers and 638657 trainable parameters. The third architecture, summarized in Table S1, is inspired by the well-known ResNet architecture (He et al., 2016). It contains a total of nine convolutional layers couched within so-called residual blocks (He et al., 2016), and 390321 trainable parameters. The residual blocks mitigate the issue of vanishing gradients during training, thereby allowing for the construction of deeper networks that often outperform their shallower counterparts. We consider ensembles containing up to 10 NBEs of θ , where each NBE is initialised with different, randomly generated values for the neural-network parameters $\boldsymbol{\gamma}$.

Table S1: Summary of the CNN architecture used in Sections 3 and 4 of the main text, and in Sections S3 and S4, with p the number of parameters in the given statistical model. The architecture can be used with grids of arbitrary size and shape; however, for simplicity, here we show the input and output dimensions of each layer given a square input grid of dimension 64×64 . The table is divided into layers used for the summary network $\psi(\cdot)$ and inference network $\phi(\cdot)$ of the DeepSets representation given in Equation (15) of the main text. Each residual block consists of two sequential convolutional layers and batch normalization layers, along with a skip (shortcut) connection that directly connects the input of the block to its output (He et al., 2016). The batch normalization layers compute the mean and variance for each input slice, normalize the input accordingly, and then apply a learnable affine transformation (Ioffe and Szegedy, 2015). A padding of size 1 is used in each convolutional layer, and a stride of 2 is used in layers that reduce the input resolution (a stride of 1 is used otherwise) (Goodfellow et al., 2016, Ch. 9). For all but the final layer, we use rectified linear unit (ReLU) activation functions, $\text{ReLU}(x) \equiv \max(0, x)$, while the final layer employs a softplus activation function, $\text{softplus}(x) \equiv \log(1 + e^x)$, to ensure positive parameter estimates. When employing the masking approach of Wang et al. (2024), an extra input channel is needed to encode the missingness pattern, which doubles the number of parameters in the first layer.

Network	Layer type	Input dim.	Output dim.	Kernel size	Parameters
$\psi(\cdot)$	Convolutional	[64, 64, 1]	[64, 64, 16]	3×3	144
$\psi(\cdot)$	Batch normalization	[64, 64, 16]	[64, 64, 16]	-	32
$\psi(\cdot)$	Residual block	[64, 64, 16]	[64, 64, 16]	3×3	4672
$\psi(\cdot)$	Residual block	[64, 64, 16]	[32, 32, 32]	3×3	14528
$\psi(\cdot)$	Residual block	[32, 32, 32]	[16, 16, 64]	3×3	57728
$\psi(\cdot)$	Residual block	[16, 16, 64]	[8, 8, 128]	3×3	230144
$\psi(\cdot)$	Global mean pooling	[8, 8, 128]	[1, 1, 128]	-	0
$\psi(\cdot)$	Flatten	[1, 1, 128]	[128]	-	0
$\phi(\cdot)$	Dense	[128]	[128]	-	16512
$\phi(\cdot)$	Dense	[128]	[512]	-	66048
$\phi(\cdot)$	Dense	[512]	[p]	-	$513p$
Total trainable parameters:					$389808 + 513p$

Figure S3 shows empirical root-mean-squared errors (RMSEs) for 10 individual NBEs and the corresponding ensemble of $J = 10$ NBEs (left panel), and empirical RMSEs as a function of the number of NBEs in the ensemble (right panel). The empirical RMSEs are based on a test set of 1000 parameter-data pairs sampled from the joint distribution of the parameters and the data, that is,

$$\text{RMSE}(\hat{\theta}(\cdot)) \equiv \sqrt{\frac{1}{1000} \sum_{j=1}^{1000} \{\hat{\theta}(\mathbf{Z}^{(k)}) - \theta^{(k)}\}^2}, \quad (\text{S7})$$

where $\theta^{(k)} \sim \text{Unif}(0, 0.5)$, $\mathbf{Z}^{(k)} \sim f_{\mathbf{Z}|\theta}(z | \theta_k)$, and the estimator $\hat{\theta}(\cdot)$ corresponds either to a single NBE or an ensemble of NBEs as defined in (S6). From Figure S3, we see that the use of an ensemble of NBEs substantially reduces the RMSE when compared to a single NBE, irrespective of the architecture. Further, our proposed ResNet-like architecture results in

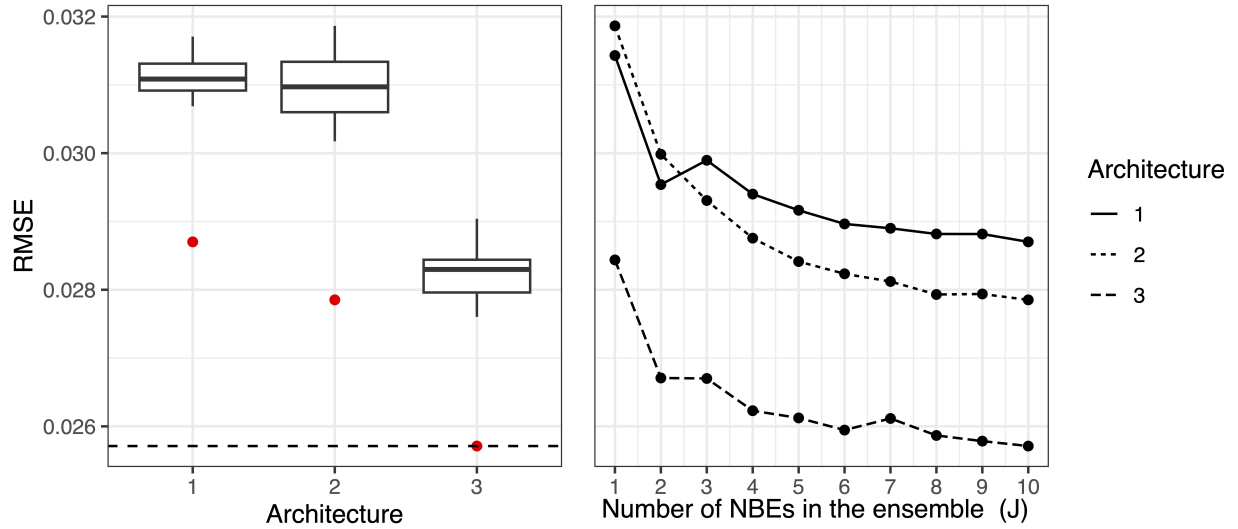


Figure S3: (Left panel) Empirical RMSEs for three different architectures, with boxplots showing the RMSEs for 10 individual NBEs, and red points showing the RMSEs of the corresponding ensemble of $J = 10$ NBEs. Here, the horizontal dashed line corresponds to the RMSE of the MAP estimator that numerically maximizes the unnormalized analytic posterior density. (Right panel) Empirical RMSEs as a function of the number of NBEs in the ensemble, for three different architectures. Architecture 3 corresponds to our proposed architecture (Table S1).

reduced RMSE in all cases.

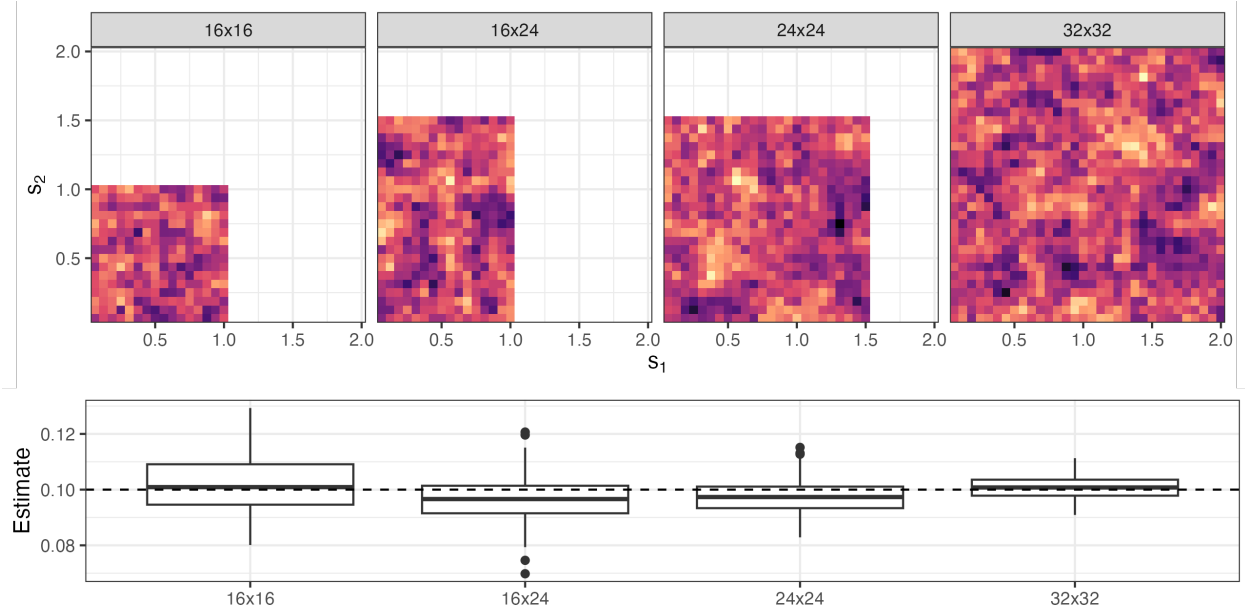


Figure S4: Simulated data sets from the Gaussian process in Section S3 (with $\theta = 0.1$) collected over grids of varying size and shape (top row) and the corresponding empirical sampling distribution (bottom row) of an ensemble of $J = 10$ NBEs that employ our proposed architecture (Table S1).

S4 Flexible neural networks for gridded data

Our proposed architecture (Table S1) incorporates a so-called global mean pooling layer (Lin et al., 2014, Section 3.2) after the convolutional layers (see the 7th line of Table S1). This layer averages over each hidden feature map generated by the convolutional layers, thereby allowing grids of arbitrary size and shape to be mapped to a fixed-length hidden-feature vector. This allows a single NBE (or an ensemble of NBEs) to be used with grids of differing size and shape, which is important in some applications.

To demonstrate this flexibility, we apply the ensemble of $J = 10$ NBEs constructed in Section S3, which were trained with spatial grids of size 16×16 , to several data sets on grids of size 16×24 , 24×24 , and 32×32 , with the spatial domain increasing in size accordingly (i.e., each pixel represents a fixed area across all cases). Figure S4 shows that the ensemble performs well in each case, with a notable reduction in uncertainty when data are collected over a larger grid.

S5 Checkerboard Gibbs sampler

Checkerboard Gibbs sampling is an algorithm for efficiently simulating from Markov-random-field (MRF) models defined on grids, such as the Potts model considered in Section 3.3 and Section 4 of the main text.

Consider a regular grid of pixels numbered $i = 1, \dots, n$ where each pixel takes on a value Z_i , which may be discrete or continuous. Now, consider a generic MRF model parameterized

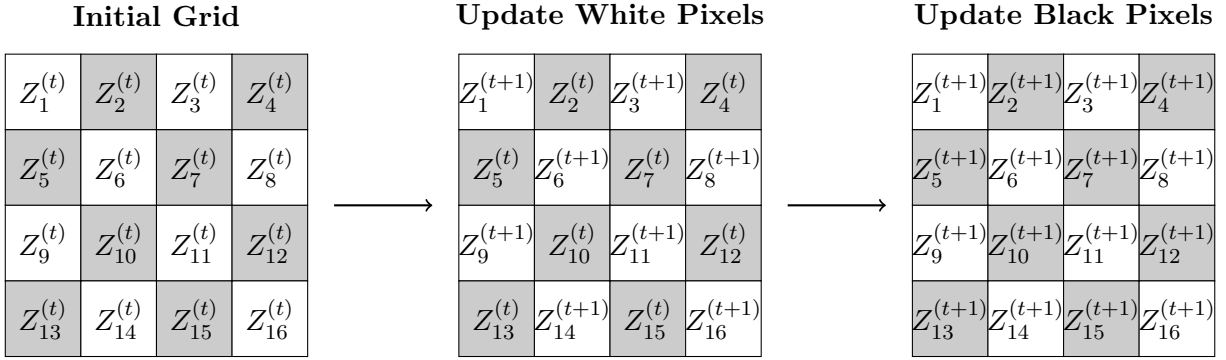


Figure S5: Illustration of a single iteration of a checkerboard Gibbs sampler on a square grid with $n = 16$ pixels. Starting with the pixel labels $\mathbf{Z}^{(t)} \equiv (Z_1^{(t)}, \dots, Z_n^{(t)})'$ (Left), the white pixel labels are updated in parallel with the black pixel labels held fixed (Center); then, the black pixel labels are updated in parallel with the white pixel labels held fixed (Right).

by $\boldsymbol{\theta}$ and characterized by the local-dependence property,

$$[Z_i \mid \mathbf{Z}_{\setminus i}, \boldsymbol{\theta}] = [Z_i \mid \mathbf{Z}_{\mathcal{N}_i}, \boldsymbol{\theta}], \quad (\text{S8})$$

where we use the square bracket notation to denote generic probability density/mass functions; for pixels $i = 1, \dots, n$, $\mathbf{Z}_{\setminus i}$ denotes all pixel labels excluding the i th pixel; \mathcal{N}_i denotes the neighbors of pixel i ; and $\mathbf{Z}_{\mathcal{N}_i}$ denotes the pixel labels of the neighbors of pixel i .

A common choice for \mathcal{N}_i is the four adjacent pixels of pixel i . In this case, the grid may be partitioned into two disjoint subsets based on a checkerboard pattern of “white” and “black” pixels, respectively denoted by $W \equiv \{i : i \text{ is odd}\}$ and $B \equiv \{i : i \text{ is even}\}$, such that all pixel labels with a given ‘color’ are conditionally independent of all other pixel labels with the same color. The conditional independence between pixels of the same color allows for an efficient Gibbs sampling algorithm, with each iteration done in two steps:

1. Sample $\mathbf{Z}_W^{(t+1)} \sim [\mathbf{Z}_W \mid \mathbf{Z}_B^{(t)}, \boldsymbol{\theta}] = \prod_{i \in W} [Z_i \mid \mathbf{Z}_{\mathcal{N}_i}^{(t)}, \boldsymbol{\theta}]$,
2. Sample $\mathbf{Z}_B^{(t+1)} \sim [\mathbf{Z}_B \mid \mathbf{Z}_W^{(t+1)}, \boldsymbol{\theta}] = \prod_{i \in B} [Z_i \mid \mathbf{Z}_{\mathcal{N}_i}^{(t+1)}, \boldsymbol{\theta}]$,

for Gibbs sampler iteration $t = 0, 1, \dots$; $\mathbf{Z}_W \equiv (Z_i : i \in W)'$ and $\mathbf{Z}_B \equiv (Z_i : i \in B)'$, respectively denote the “white” and “black” pixel labels; and initial values $\mathbf{Z}_W^{(0)}$ and $\mathbf{Z}_B^{(0)}$ are required. Figure S5 illustrates a single iteration of a checkerboard Gibbs sampler for a square grid with $n = 16$ pixels.

S6 Application to cryptocurrency data

To further demonstrate the applicability of the neural-network-based estimation approaches discussed in the main text, this time for data that are low-dimensional, here we use the generalized hyperbolic distribution (described in Section S6.1) and NBEs to analyze cryptocurrency data (Section S6.2).

S6.1 Generalized hyperbolic distribution

The n -dimensional random variable \mathbf{Z} is called a normal mean-variance mixture (NMVM) if it can be represented as,

$$\mathbf{Z} = \boldsymbol{\mu} + M\boldsymbol{\alpha} + \sqrt{M}\mathbf{V}, \quad (\text{S9})$$

where $\boldsymbol{\mu} \in \mathbb{R}^n$, $\boldsymbol{\alpha} \in \mathbb{R}^n$, M is a positive (mixing) random variable that is independent of the small-scale variation $\mathbf{V} \sim \text{Gau}(\mathbf{0}, \boldsymbol{\Sigma})$, and where $\boldsymbol{\Sigma}$ is a covariance matrix. This family of distributions is closed under conditioning: for any partitioning of \mathbf{Z} into components \mathbf{Z}_1 and \mathbf{Z}_2 , and with $\boldsymbol{\mu}$, $\boldsymbol{\alpha}$, and $\boldsymbol{\Sigma}$ partitioned accordingly, $\mathbf{Z}_2 \mid \mathbf{Z}_1$ is also a NMVM, with parameters

$$\begin{aligned} \boldsymbol{\mu}_{2|1} &= \boldsymbol{\mu}_2 + \boldsymbol{\Sigma}_{21}\boldsymbol{\Sigma}_{11}^{-1}(\mathbf{Z}_1 - \boldsymbol{\mu}_1), \\ \boldsymbol{\alpha}_{2|1} &= \boldsymbol{\alpha}_2 - \boldsymbol{\Sigma}_{21}\boldsymbol{\Sigma}_{11}^{-1}\boldsymbol{\alpha}_1, \\ \boldsymbol{\Sigma}_{22|1} &= \boldsymbol{\Sigma}_{22} - \boldsymbol{\Sigma}_{21}\boldsymbol{\Sigma}_{11}^{-1}\boldsymbol{\Sigma}_{12}, \end{aligned}$$

and with mixing variable $M_{2|1}$ that is distributed according to $M \mid \mathbf{Z}_1$ (Jamalizadeh and Balakrishnan, 2019, Theorem 1).

The generalized hyperbolic (GH) distribution is obtained when M in (S9) follows a generalized inverse Gaussian (GIG) distribution. We consider the parameterization of the GIG density employed by Browne and McNicholas (2015),

$$f_{\text{GIG}}(m; \omega, \phi, \lambda) = \frac{(m/\phi)^{\lambda-1}}{2\phi K_\lambda(\omega)} \exp\left\{-\frac{\omega}{2}\left(\frac{\phi}{m} + \frac{m}{\phi}\right)\right\}, \quad m > 0, \quad (\text{S10})$$

with concentration parameter $\omega > 0$, shape parameter $\lambda \in \mathbb{R}$, scale parameter $\phi > 0$, and where $K_\lambda(\cdot)$ denotes the modified Bessel function of the second kind of order λ . Then, $M_{2|1}$ also follows a GIG distribution with parameters

$$\begin{aligned} \omega_{2|1} &= \sqrt{\{\omega\phi + (\mathbf{Z}_1 - \boldsymbol{\mu}_1)' \boldsymbol{\Sigma}_{11}^{-1} (\mathbf{Z}_1 - \boldsymbol{\mu}_1)\} \{\omega\phi^{-1} + \boldsymbol{\alpha}_1' \boldsymbol{\Sigma}_{11}^{-1} \boldsymbol{\alpha}_1\}}, \\ \phi_{2|1} &= \sqrt{\{\omega\phi + (\mathbf{Z}_1 - \boldsymbol{\mu}_1)' \boldsymbol{\Sigma}_{11}^{-1} (\mathbf{Z}_1 - \boldsymbol{\mu}_1)\} / \{\omega\phi^{-1} + \boldsymbol{\alpha}_1' \boldsymbol{\Sigma}_{11}^{-1} \boldsymbol{\alpha}_1\}}, \\ \lambda_{2|1} &= \lambda - n_1/2, \end{aligned}$$

where n_1 is the dimension of \mathbf{Z}_1 (Jamalizadeh and Balakrishnan, 2019, Cor. 2). Throughout, we fix $\phi = 1$ for identifiability reasons.

The GH distribution is prominent in financial modeling due to its flexible marginal distributions and infinite divisibility (Barndorff-Nielsen, 1997; Prause, 1999). We write

$\mathbf{Z} \sim \text{GH}(\boldsymbol{\mu}, \boldsymbol{\alpha}, \boldsymbol{\Sigma}, \omega, \phi, \lambda)$, which has density function,

$$f_{\text{GH}}(\mathbf{z}; \boldsymbol{\mu}, \boldsymbol{\alpha}, \boldsymbol{\Sigma}, \omega, \phi, \lambda) \propto \frac{K_{\lambda-d/2} \left(\sqrt{\{\omega\eta + (\mathbf{z} - \boldsymbol{\mu})' \boldsymbol{\Sigma}^{-1} (\mathbf{z} - \boldsymbol{\mu})\} (\omega/\eta + \boldsymbol{\gamma}' \boldsymbol{\Sigma}^{-1} \boldsymbol{\gamma})} \right) e^{(\mathbf{z} - \boldsymbol{\mu})' \boldsymbol{\Sigma}^{-1} \boldsymbol{\alpha}}}{\left[\sqrt{\{\omega\eta + (\mathbf{z} - \boldsymbol{\mu})' \boldsymbol{\Sigma}^{-1} (\mathbf{z} - \boldsymbol{\mu})\} (\omega/\eta + \boldsymbol{\gamma}' \boldsymbol{\Sigma}^{-1} \boldsymbol{\gamma})} \right]^{n/2-\lambda}},$$

with normalizing constant, $(\omega\phi^{-1} + \boldsymbol{\alpha}' \boldsymbol{\Sigma}^{-1} \boldsymbol{\alpha})^{n/2-\lambda} (2\pi)^{-n/2} |\boldsymbol{\Sigma}|^{-1/2} \phi^{-\lambda} / K_{\lambda}(\omega)$ (McNeil et al., 2015, Eqn. 6.29; Zhang et al., 2022). In addition to being closed under conditioning, the GH family of distributions is also closed under marginalization (Wei et al., 2019, Prop. 2). That is, if $\mathbf{Z} \equiv (\mathbf{Z}'_1, \mathbf{Z}'_2)' \sim \text{GH}(\boldsymbol{\mu}, \boldsymbol{\alpha}, \boldsymbol{\Sigma}, \omega, \phi, \lambda)$, then $\mathbf{Z}_1 \sim \text{GH}(\boldsymbol{\mu}_1, \boldsymbol{\alpha}_1, \boldsymbol{\Sigma}_{11}, \omega, \phi, \lambda)$. Therefore, although the likelihood function is available, likelihood-based estimators for the GH distribution require repeated evaluation of the Bessel function, which can be computationally burdensome. Likelihood-free methods may therefore improve computational efficiency with little decrease in statistical efficiency.

The tail properties of the GH distribution have been well studied, most recently by Zhang et al. (2022). Here, for simplicity, we present tail properties for $\mathbf{Z} \equiv (Z_1, Z_2)' \sim \text{GH}(\boldsymbol{\mu}, \boldsymbol{\alpha}, \boldsymbol{\Sigma}, \phi, \omega, \lambda)$. The elements Z_1 and Z_2 are asymptotically independent, that is,

$$\lim_{u \rightarrow 1} \Pr(U_1 > u \mid U_2 > u) = 0,$$

where, for $i \in \{1, 2\}$, $U_i \equiv F_i(Z_i)$ and $F_i(\cdot)$ denotes the marginal distribution function of Z_i (Zhang et al., 2022). The extremal dependence strength at sub-asymptotic levels can be quantified using the residual-tail-dependence coefficient (Ledford and Tawn, 1996), also known as the coefficient of tail dependence, which is defined through the limit,

$$\eta = \lim_{u \rightarrow 1} \frac{\log \Pr(U_1 > u)}{\log \Pr(U_1 > u, U_2 > u)}. \quad (\text{S11})$$

The coefficient η takes values between 0 and 1, and characterizes the rate of tail decay towards independence. Smaller values indicate faster decay, while larger values correspond to slower decay. For the GH distribution, the coefficient is available in closed form,

$$\eta = \left\{ \left((\omega/\phi + \boldsymbol{\alpha}' \boldsymbol{\Sigma}^{-1} \boldsymbol{\alpha}) \boldsymbol{\beta}' \boldsymbol{\Sigma}^{-1} \boldsymbol{\beta} \right)^{1/2} - \boldsymbol{\beta}' \boldsymbol{\Sigma}^{-1} \boldsymbol{\alpha} \right\}^{-1}, \quad (\text{S12})$$

where $\boldsymbol{\beta} \equiv (\beta_1, \beta_2)'$ and $\beta_i \equiv \phi \{ \alpha_i + (\omega/\phi + \alpha_i^2)^{1/2} \} / \omega$, $i = 1, 2$ (Zhang et al., 2022).

S6.2 Analysis of returns from Bitcoin, Ethereum, and Avalanche

We now consider an analysis of cryptocurrency data. The statistical modeling of extreme events plays an important role in financial risk assessment when investing in these decentralized digital currencies. Here, we analyze the probability of simultaneous extreme events (profits or losses) from three leading cryptocurrencies: Bitcoin, Ethereum, and Avalanche.

Bitcoin and Ethereum are, at the time of writing, the two largest cryptocurrencies by market capitalization, while Avalanche is a more recent cryptocurrency that ranks 13th by market capitalization. Figure S6 (left column) shows the historical daily closing prices of these coins

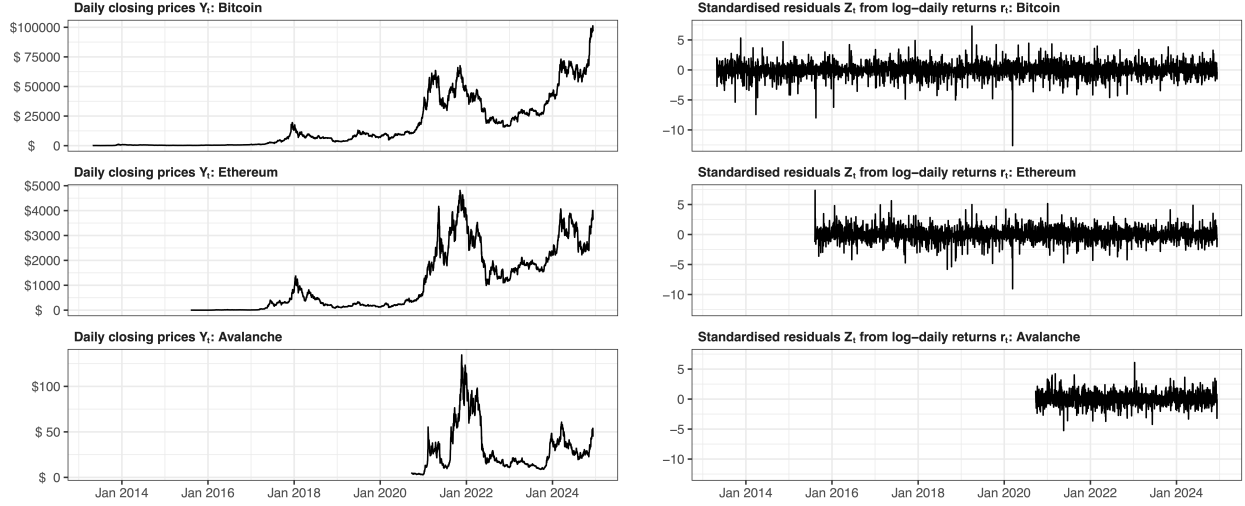


Figure S6: Historical daily closing prices in US dollars (Left) and standardized residuals (Right) extracted from fitting an ARMA(1,1)–GARCH(1,1) model to the log returns of the cryptocurrencies Bitcoin, Ethereum, and Avalanche.

from April 28, 2013 to December 10, 2024, obtained from <https://coinmarketcap.com> using the package **crypto2** (Stoeckl, 2024). The joint modeling of these data is complicated by the differing inception dates of each coin, which creates temporally structured missingness. We first fit a time-series models to the log returns of each cryptocurrency using an ARMA(1,1)–GARCH(1,1) model (Spierdijk, 2016; Gong and Huser, 2022). Specifically, the log returns $r_t \equiv \ln(Y_t/Y_{t-1})$ from closing prices Y_t , $t = t_0, \dots, T$, are modeled as:

$$\begin{aligned} r_t &= \mu_t + \sigma_t X_t, \\ \mu_t &= a + br_{t-1} + c(r_{t-1} - \mu_{t-1}), \\ \sigma_t^2 &= d + e(r_{t-1} - \mu_{t-1})^2 + f\sigma_{t-1}^2, \end{aligned}$$

where the starting time t_0 varies by cryptocurrency ($t_0 = 1$ for Bitcoin, $t_0 = 832$ for Ethereum, and $t_0 = 2705$ for Avalanche), $T = 4244$ denotes the number of days between April 28, 2013 to December 10, 2024, $X_t \sim \text{Gau}(0, 1)$, and the model parameters are $a \in \mathbb{R}$, $|b| < 1$, $c \in \mathbb{R}$, $d > 0$, $e \geq 0$, and $f \geq 0$.

We fit the model to each time series separately using the package **rugarch** (Galanos, 2024) and, from these fits, we derive standardized residuals $Z_t \equiv (r_t - \hat{\mu}_t)/\hat{\sigma}_t$, where $\hat{\mu}_t$ and $\hat{\sigma}_t$ denote the estimated conditional mean and standard deviation (volatility) of the log returns, respectively, calculated using estimated parameters \hat{a} , \hat{b} , \hat{c} , \hat{d} , \hat{e} , and \hat{f} . We denote the standardized residuals for the three cryptocurrencies by $\mathbf{Z}_t \equiv (Z_{t1}, Z_{t2}, Z_{t3})'$, $t = 1, \dots, T$, with components corresponding to times preceding a coin's inception date treated as missing. These residuals, which form the basis of our subsequent analyses, are shown in Figure S6 (right column) and Figure S7.

We assume that the residuals \mathbf{Z}_t , $t = 1, \dots, T$, are mutually independent and identically distributed, although dependence is present within each trivariate vector. We simplify notation by writing $\mathbf{Z} \equiv (Z_1, Z_2, Z_3)'$ to represent a generic standardized residual. We model

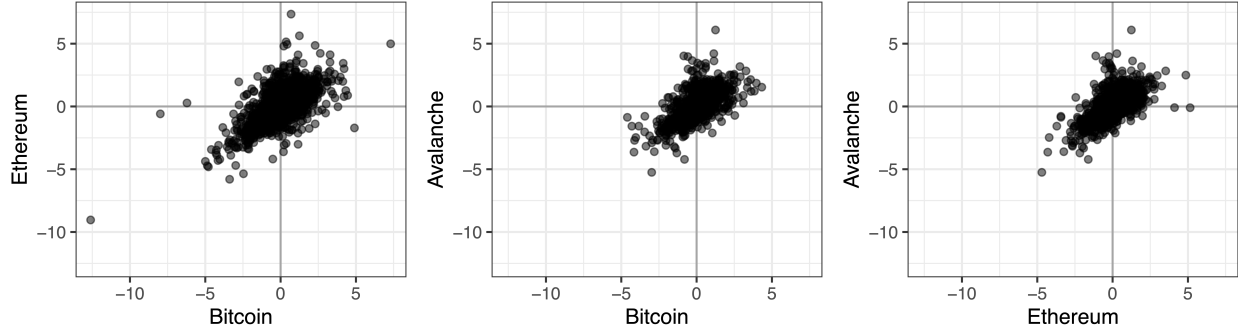


Figure S7: Bivariate standardized residuals extracted from fitting an ARMA(1,1)–GARCH(1,1) model to the log returns of the cryptocurrencies Bitcoin, Ethereum, and Avalanche.

\mathbf{Z} using a trivariate GH distribution where, in (S9), we set $\boldsymbol{\mu} = \mathbf{0}$; we set $\boldsymbol{\alpha} = \alpha \mathbf{1}$; and we take the diagonal elements of $\boldsymbol{\Sigma}$ to be 1. This leaves six parameters to be estimated: $\boldsymbol{\theta} \equiv (\alpha, \lambda, \omega, \Sigma_{21}, \Sigma_{31}, \Sigma_{32})'$. We assume that α , ω , and λ are mutually independent a priori and independent of $\boldsymbol{\Sigma}$, and we use the marginal priors $\alpha \sim \text{Unif}(-0.3, 0.3)$, $\omega \sim \text{Unif}(0, 1)$, and $\lambda \sim \text{Unif}(-1, 1)$. For $\boldsymbol{\Sigma}$, we use a prior that is uniform over all permissible correlation matrices (Lewandowski et al., 2009).

To make parameter inference from the standardized residuals, we use NBEs that employ either the masking approach (Algorithm 1 of the main text) or the EM approach (Algorithm 2 of the main text), and we refer to these estimators as a “Masking NBE” and an “EM NBE,” respectively. For validation, we employ conventional MAP estimation by maximizing the unnormalized analytic posterior density obtained from the likelihood function f_{GH} given in Section S6.1 and our specification of prior distributions. Since the data are multivariate and unstructured, we use a fully-connected neural-network architecture summarized in Table S2. When training the Masking NBE, we use an MCAR model for the missingness mechanism, with the missingness proportions drawn from the $\text{Unif}(0, 1)$ distribution. The total training time (including data simulation) for the Masking NBE and EM NBE was 2.2 hours and 1.3 hours, respectively. During the estimation stage of Algorithm 2 of the main text, we set $H = 1$, and the computation times are given below.

Table S3 gives GH parameter estimates and 95% confidence intervals for the three estimators. The confidence intervals were computed using a non-parametric bootstrap approach. Specifically, 400 bootstrap data sets were generated by resampling the standardized residuals with replacement, justified by the residuals being independent after the temporal dependence was removed by initially fitting an ARMA(1,1)–GARCH(1,1) model. The estimators were then applied to each data set, and the 0.025 and 0.975 quantiles of the resulting bootstrap distributions were used to construct the intervals. The estimates given in Table S3 are in overall agreement. The average run time per estimate for the MAP estimate, EM NBE, and Masking NBE was 2.67 seconds, 0.081 seconds, and 0.001 seconds, respectively. As in Section 3 of the main text, we see that the neural-network-based estimators are orders of magnitude faster than the likelihood-based estimator, which we could compute in this instance.

We validated the fitted models by comparing empirical and model-based estimates of joint tail dependence. For simplicity, we focused on bivariate measures of tail dependence. (Recall

Table S2: Summary of the neural-network architecture used in the EM NBE in Section S6.2, where p denotes the number of parameters (in this case, $p = 6$). The table is divided into layers used for the summary network $\psi(\cdot)$ and inference network $\phi(\cdot)$ of the DeepSets representation given in Equation (15) of the main text. A padding of 0 and a stride of 1 was used in each convolutional layer. We used the cube-root function as a variance-stabilizing transformation before passing the data into the network. For all layers except the final layer, we used ReLU activation functions. For the final layer, we used an identity function for real-valued parameters, a softplus activation function for positive parameters and, for correlation-matrix parameters, the bijective mapping between real-valued inputs and valid correlation-matrix parameters given by Lewandowski et al. (2009). When employing the Masking NBE, we use a bilinear layer (Tenenbaum and Freeman, 2000) with 1280 trainable parameters for the first layer.

Network	Layer type	Input dimension	Output dimension	Parameters
$\psi(\cdot)$	Dense	[3]	[128]	512
$\psi(\cdot)$	Dense	[128]	[128]	16512
$\psi(\cdot)$	Dense	[128]	[256]	33024
$\phi(\cdot)$	Dense	[256]	[128]	32896
$\phi(\cdot)$	Dense	[128]	[128]	16512
$\phi(\cdot)$	Dense	[128]	[p]	$129p$
Total trainable parameters:				$99456 + 129p$

Table S3: GH parameter estimates and 95% bootstrap confidence intervals (in parentheses) for the cryptocurrency data set of Section S6.2.

Parameter	MAP	EM NBE	Masking NBE
α	0.00 (-0.03, 0.02)	0.00 (-0.03, 0.03)	0.00 (-0.02, 0.03)
ω	0.44 (0.38, 0.49)	0.51 (0.43, 0.61)	0.52 (0.45, 0.60)
λ	-0.43 (-0.48, -0.39)	-0.46 (-0.52, -0.39)	-0.47 (-0.53, -0.40)
Σ_{21}	0.71 (0.70, 0.73)	0.72 (0.69, 0.74)	0.73 (0.72, 0.74)
Σ_{31}	0.62 (0.59, 0.65)	0.66 (0.62, 0.70)	0.67 (0.62, 0.70)
Σ_{32}	0.67 (0.63, 0.70)	0.64 (0.60, 0.68)	0.71 (0.68, 0.73)

that the GH distribution is closed under marginalization, which allows us to obtain the three bivariate distributions from the trivariate fit.) For $i = 1, 2, 3$, let $F_i(\cdot)$ denote the marginal distribution function of Z_i (the standardized residual of the i th cryptocurrency), and define the uniformly distributed random variable $U_i \equiv F_i(Z_i)$. A natural quantity of interest is the joint lower-tail probability, $\Pr(U_i < u, U_j < u)$ for $i < j = 2, 3$ and threshold u close to zero, which corresponds to the probability of simultaneous extreme losses for each pair of cryptocurrencies. Figure S8 shows the estimated joint lower-tail probabilities for all three pairs of cryptocurrencies and threshold $u \in (0, 0.1)$. The green and blue lines denote model-based estimates using GH model fits obtained with the EM NBE and the Masking NBE, respectively; the black line denotes the empirical estimate obtained from bivariate empirical distribution functions; and shaded areas display 95% pointwise confidence intervals, obtained using non-parametric bootstrap sampling as described above. In Figure S8, we omit results for the MAP estimate to prevent overplotting. Visually, there appears to be some minor discrepancy between empirical and model-based estimates, but all lines are within the 95%

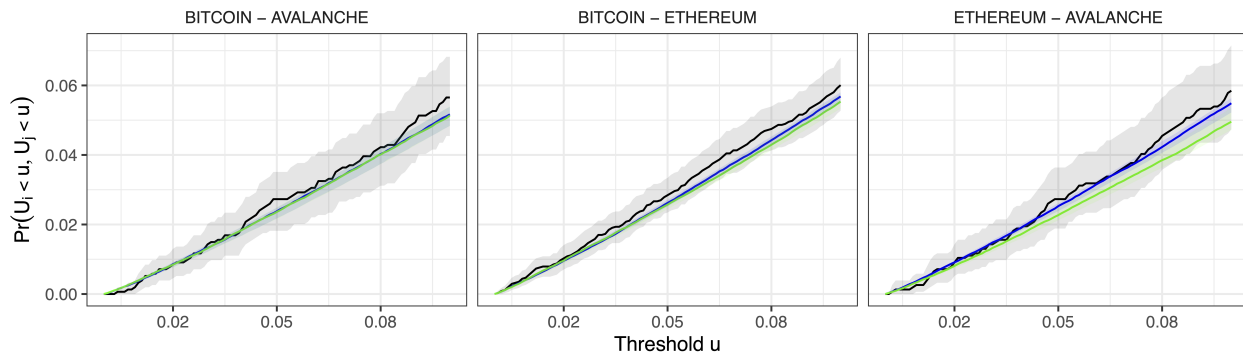


Figure S8: Joint lower-tail probabilities $\Pr(U_i < u, U_j < u)$, $i < j = 2, 3$, for threshold $u \in (0, 0.1)$, estimated for all pairs of cryptocurrencies. The green and blue lines denote model-based estimates using model fits obtained with the EM NBE and the Masking NBE, respectively. The black line denotes the empirical estimate. Shaded areas display 95% pointwise confidence intervals obtained using non-parametric bootstrap sampling.

Table S4: Estimates and 95% bootstrap confidence intervals of the bivariate residual-tail-dependence coefficients for each pair of cryptocurrencies.

Coefficient	MAP	Neural EM	Masked NBE
$\eta_{\text{BTC-ETH}}$	0.93 (0.92, 0.94)	0.93 (0.92, 0.94)	0.93 (0.92, 0.94)
$\eta_{\text{BTC-AVL}}$	0.90 (0.89, 0.91)	0.91 (0.90, 0.92)	0.91 (0.90, 0.92)
$\eta_{\text{ETH-AVL}}$	0.91 (0.90, 0.92)	0.90 (0.89, 0.92)	0.92 (0.91, 0.93)

shaded areas. On the whole, the models seem to be a reasonable fit to this data set.

To further quantify the extremal dependence strength, we also consider the bivariate residual-tail-dependence coefficient defined by (S11) for each pair of cryptocurrencies. Specifically, we use the formula (S12) to provide model-based estimates of the bivariate residual-tail-dependence coefficient for each pair of cryptocurrencies. We denote these by $\eta_{\text{BTC-ETH}}$, $\eta_{\text{BTC-AVL}}$, and $\eta_{\text{ETH-AVL}}$ for the Bitcoin-Ethereum pair, the Bitcoin-Avalanche pair, and the Ethereum-Avalanche pair, respectively. Point estimates and confidence intervals of these three coefficients are given in Table S4. These consistently large estimates imply that the tail dependence is quite strong for each cryptocurrency pair, suggesting that extreme events may often occur simultaneously.

S7 Additional figures

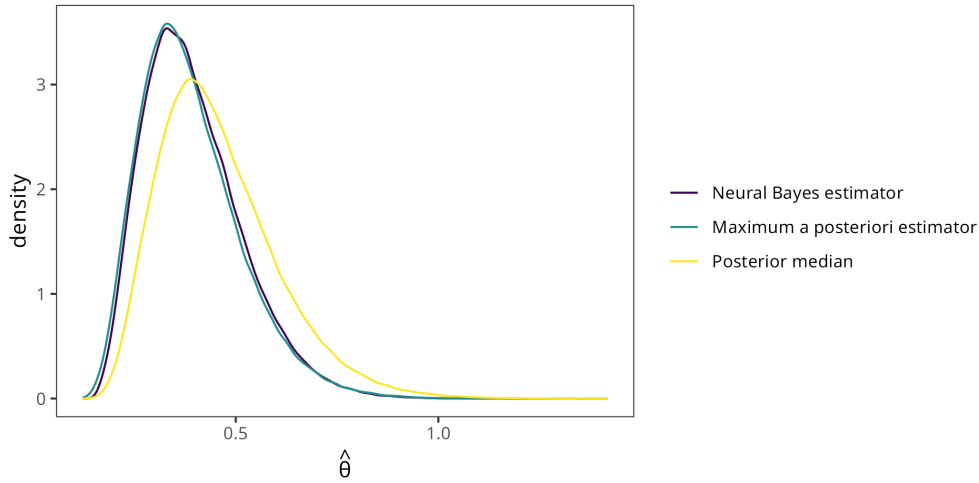


Figure S9: (For Section 2.3.3 of the main text.) Kernel-smoothed sampling distributions of an NBE trained to approximate the MAP estimator, of the analytic MAP estimator, and of the posterior median, from data $\mathbf{Z} \equiv (Z_1, \dots, Z_{10})'$ where, for $i = 1, \dots, 10$, $Z_i \stackrel{\text{iid}}{\sim} \text{Gau}(0, \theta)$, and $\theta = 0.5$. The prior for θ is taken to be inverse gamma with shape $\alpha = 3$ and rate $\beta = 1$. The posterior distribution of θ is also inverse gamma, with shape $\tilde{\alpha} = \alpha + n/2$ and rate $\tilde{\beta} = \beta + \sum_{i=1}^m Z_i^2/2$. For this model, the analytic MAP estimate is $\tilde{\beta}(\tilde{\alpha} + 1)^{-1}$ and, while the posterior median is unavailable in closed form, it can be accurately approximated through simulation. The NBE is trained with $K = 10000$ and $\kappa = 0.05$ in Equations (3) and (14) of the main text, respectively.

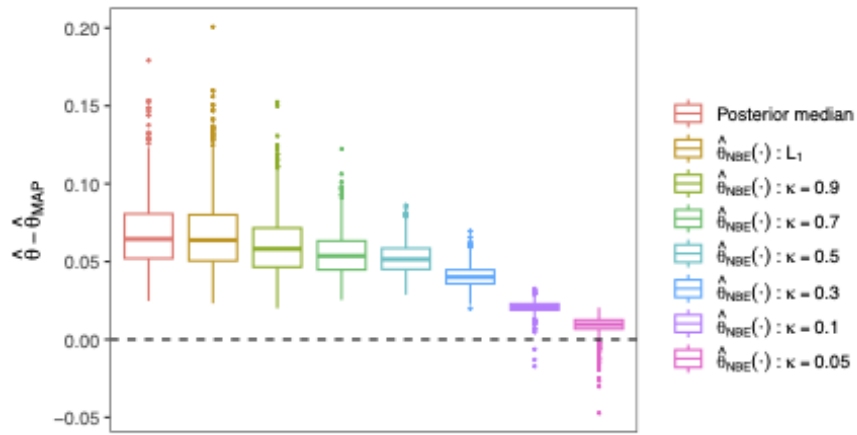


Figure S10: (For Section 2.3.3 of the main text.) Differences between several estimators and the MAP estimator from data $\mathbf{Z} \equiv (Z_1, \dots, Z_{10})'$ where, for $i = 1, \dots, 10$, $Z_i \stackrel{\text{iid}}{\sim} \text{Gau}(0, \theta)$, $\theta = 0.5$, and the prior is as given in the caption of Figure S9. The estimators are the posterior median and several NBEs: one trained under the absolute-error (L_1) loss, and others trained under the continuous approximation to the 0–1 loss function given in Equation (14) of the main text for several values of κ . As κ becomes small, the resulting NBE approaches the MAP estimator.

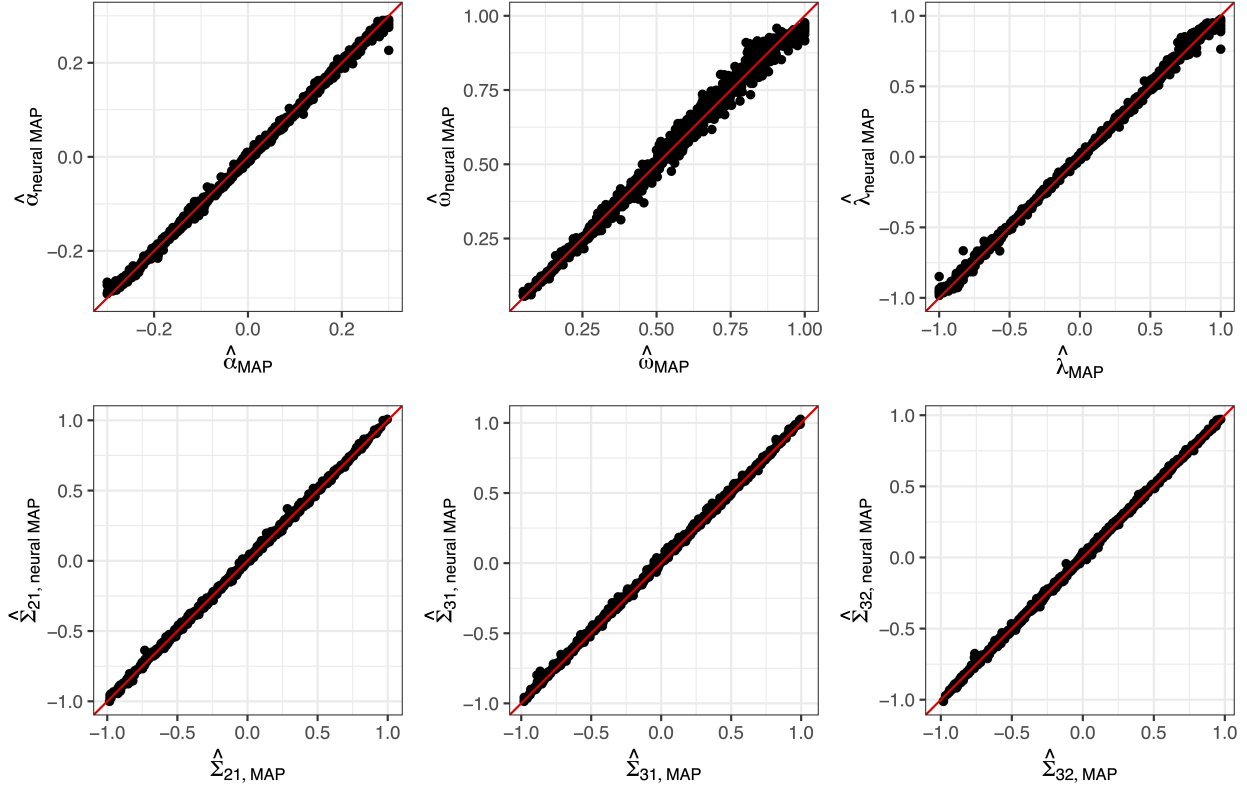


Figure S11: (For Section S6.2.) Estimates from the neural MAP estimator used in Algorithm 2 of the main text versus MAP estimates obtained by numerically maximizing the unnormalized posterior density. Each point corresponds to a pair of estimates from $HT = T = 4244$ completely observed independent replicates from the GH distribution in Section S6.2. These points provide an indication of the accuracy of each EM update in Equation (12) of the main text when approximated using the neural MAP estimator.

References

- Barndorff-Nielsen, O. (1997). Normal inverse Gaussian distributions and stochastic volatility modelling. *Scandinavian Journal of Statistics*, 24:1–13.
- Breiman, L. (1996). Bagging predictors. *Machine Learning*, 24:123–140.
- Browne, R. P. and McNicholas, P. D. (2015). A mixture of generalized hyperbolic distributions. *The Canadian Journal of Statistics*, 43:176–198.
- Casella, G. and Berger, R. (2001). *Statistical Inference*, 2nd edition. Duxbury, Belmont, CA.
- Cressie, N. (2022). Decisions, decisions, decisions in an uncertain environment. *Environmetrics*, 34:e2767.
- Dumoulin, V. and Visin, F. (2016). A guide to convolution arithmetic for deep learning. <https://doi.org/10.48550/arXiv.1603.07285>.
- Galanos, A. (2024). *rugarch: Univariate GARCH models*. R package version 1.5.3.
- Gerber, F. and Nychka, D. W. (2021). Fast covariance parameter estimation of spatial Gaussian process models using neural networks. *Stat*, 10:e382.
- Gneiting, T. and Schlather, M. (2004). Stochastic models that separate fractal dimension and the Hurst effect. *SIAM Review*, 46:269–282.
- Gong, Y. and Huser, R. (2022). Asymmetric tail dependence modeling, with application to cryptocurrency market data. *The Annals of Applied Statistics*, 16:1822–1847.
- Goodfellow, I., Bengio, Y., and Courville, A. (2016). *Deep Learning*. MIT Press, Cambridge, MA. <http://www.deeplearningbook.org>.
- Hansen, L. K. and Salamon, P. (1990). Neural network ensembles. *IEEE Transactions on Pattern Analysis and Machine Intelligence*, 12:993–1001.
- He, K., Zhang, X., Ren, S., and Sun, J. (2016). Deep residual learning for image recognition. In *Proceedings of the IEEE Conference on Computer Vision and Pattern Recognition (CVPR)*, pages 770–778.
- Ioffe, S. and Szegedy, C. (2015). Batch normalization: Accelerating deep network training by reducing internal covariate shift. In Bach, F. and Blei, D., editors, *Proceedings of the 32nd International Conference on Machine Learning*, volume 37 of *Proceedings of Machine Learning Research*, pages 448–456.
- Jamalizadeh, A. and Balakrishnan, N. (2019). Conditional distributions of multivariate normal mean-variance mixtures. *Statistics and Probability Letters*, 145:312–316.
- Ledford, A. and Tawn, J. (1996). Statistics for near independence in multivariate extreme values. *Biometrika*, 83:169–187.
- Lewandowski, D., Kurowicka, D., and Joe, H. (2009). Generating random correlation matrices based on vines and extended onion method. *Journal of Multivariate Analysis*, 100:1989–2001.
- Lin, M., Chen, Q., and Yan, S. (2014). Network in network. <https://doi.org/10.48550/arXiv.1312.4400>.
- McNeil, A. J., Frey, R., and Embrechts, P. (2015). *Quantitative Risk Management*, revised edition. Princeton University Press, Princeton, NJ.
- Prause, K. (1999). *The Generalized Hyperbolic Model: Estimation, Financial Derivatives, and Risk Measures*. PhD thesis, Albert-Ludwigs-Universität Freiburg, Germany.
- Richards, J., Sainsbury-Dale, M., Huser, R., and Zammit-Mangion, A. (2025). Neural Bayes estimators for censored inference with peaks-over-threshold models. *Journal of Machine Learning Research*, to appear. <https://doi.org/10.48550/arXiv.2306.15642>.
- Sainsbury-Dale, M., Zammit-Mangion, A., and Huser, R. (2024). Likelihood-free parameter estimation with neural Bayes estimators. *The American Statistician*, 78:1–14.

- Spierdijk, L. (2016). Confidence intervals for ARMA–GARCH value-at-risk: The case of heavy tails and skewness. *Computational Statistics and Data Analysis*, 100:545–559.
- Stoeckl, S. (2024). *crypto2: Download Crypto Currency Data from ‘CoinMarketCap’ without ‘API’*. R package version 2.0.3.
- Tenenbaum, J. B. and Freeman, W. T. (2000). Separating style and content with bilinear models. *Neural Computation*, 12:1247–1283.
- Wang, Z., Hasenauer, J., and Schälte, Y. (2024). Missing data in amortized simulation-based neural posterior estimation. *PLOS Computational Biology*, 20:e1012184.
- Wei, Y., Tang, Y., and McNicholas, P. D. (2019). Mixtures of generalized hyperbolic distributions and mixtures of skew-t distributions for model-based clustering with incomplete data. *Computational Statistics & Data Analysis*, 130:18–41.
- Zammit-Mangion, A., Sainsbury-Dale, M., and Huser, R. (2025). Neural methods for amortized inference. *Annual Review of Statistics and Its Application*, to appear. <https://doi.org/10.48550/arXiv.2404.12484>.
- Zhang, Z., Huser, R., Opitz, T., and Wadsworth, J. (2022). Modeling spatial extremes using normal mean-variance mixtures. *Extremes*, 25:175–197.